NASA Technical Paper 3205

July 1992

Validation of Three-Dimensional Incompressible Spatial Direct Numerical Simulation Code

A Comparison With Linear Stability and Parabolic Stability Equation Theories for Boundary-Layer Transition on a Flat Plate

Ronald D. Joslin,
Craig L. Streett,
and Chau-Lyan Chang

NASA

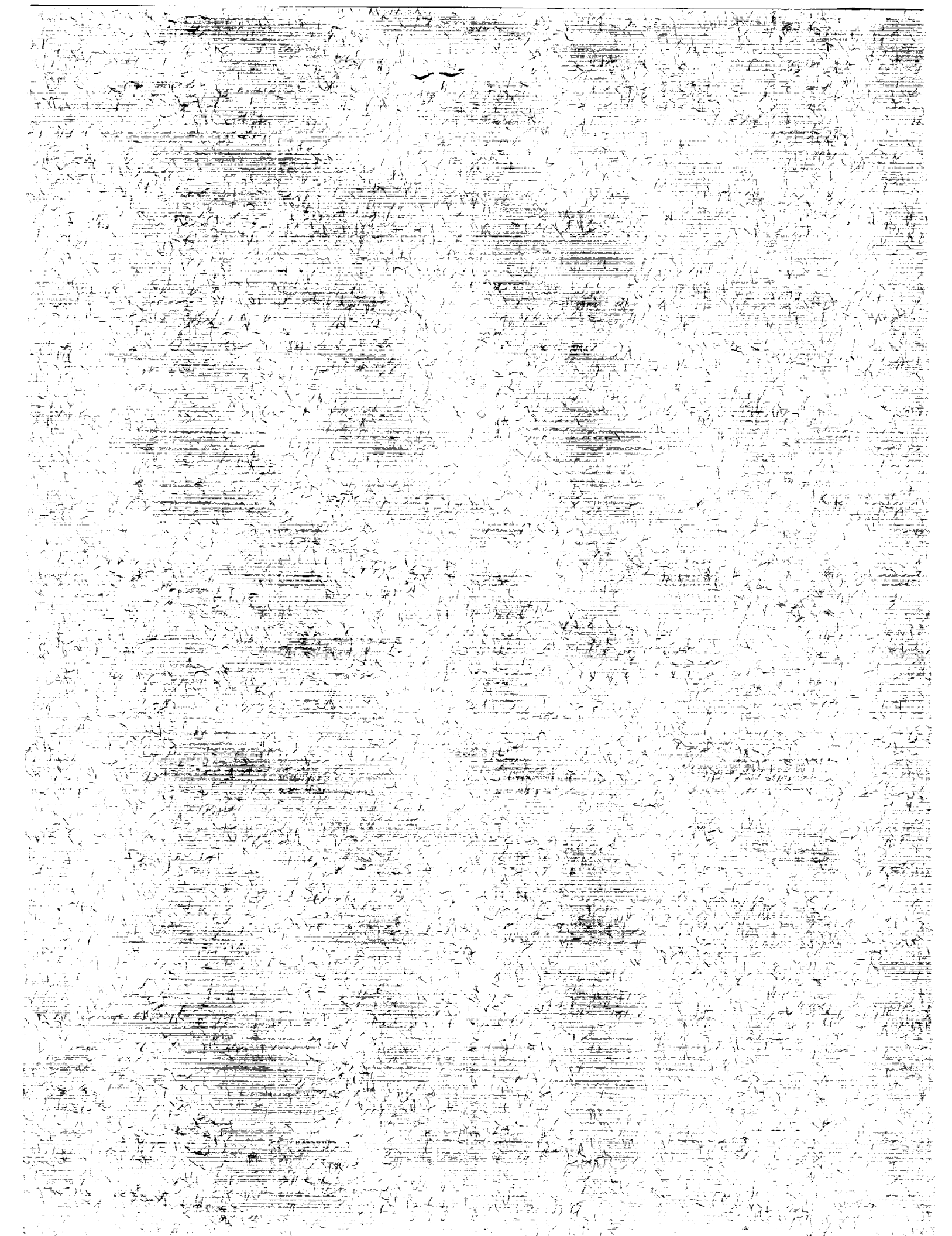

NASA Technical Paper 3205

1992

Validation of Three-Dimensional Incompressible Spatial Direct Numerical Simulation Code

A Comparison With Linear Stability and Parabolic Stability Equation Theories for Boundary-Layer Transition on a Flat Plate

Ronald D. Joslin
and Craig L. Streett
Langley Research Center
Hampton, Virginia

Chau-Lyan Chang
High Technology Corporation
Hampton, Virginia

NASA
National Aeronautics and Space Administration
Office of Management
Scientific and Technical Information Program

Summary

Spatially evolving instabilities in a flat-plate boundary layer are computed by direct numerical simulation (DNS) of the incompressible Navier-Stokes equations. In a truncated physical domain, a nonstaggered mesh is used for the grid. A Chebyshev-collocation method is used normal to the wall, fourth-order finite differences for the pressure equation and fourth-order compact differences for the momentum equations are used in the streamwise direction, and a Fourier series is used in the spanwise direction. For time stepping, implicit Crank-Nicolson and explicit Runge-Kutta schemes are used for the time-splitting method. The influence-matrix technique is used to solve the pressure equation. At the outflow boundary, the buffer-domain technique is used to prevent convective wave reflection or upstream propagation of information from the boundary. Of the techniques available to force transition, the present investigation uses approximations from linear stability theory (LST) and the newly developed parabolized stability equation (PSE) theory for inflow forcing. Comparisons are made to (1) validate the numerical techniques, (2) determine the effects of grid resolution on the downstream evolving flow, (3) determine the effects of physical domain truncation on the disturbance, (4) determine the sensitivity of the disturbances to changes in the inflow forcing, (5) test the outflow boundary condition, and (6) test the accuracy of PSE theory. The answers to the above objectives would serve as a guide for future DNS and PSE studies of more complex problems of interest with an a priori knowledge of the preceding numerical effects. As a note, the present study is concerned with unbounded flow transition. Although the related problem of bounded flows may be solved in a similar manner, the discussion (and references) in the present paper are, for the most part, confined to unbounded flows.

Results from the simulations are first compared with those of LST with a parallel mean flow used. The computed disturbance amplitudes and phases are in very good agreement with those of LST (for small inflow disturbance amplitudes). Simulations are repeated with a nonparallel mean flow. The expected increase in growth rate and wavelength shift are observed when compared with the parallel mean flow case. A comparison is also made between results from PSE theory and DNS. A measure of the sensitivity of the inflow condition is demonstrated with both LST and PSE theory used to approximate inflows on "coarse" and "fine" grids. Very small differences at the inflow are amplified downstream. Although the DNS numerics are far removed from PSE theory, the results agree relatively well. Finally, a small-amplitude wave triad is forced at the inflow, and simulation results are compared with those of LST to verify the accuracy of the three-dimensional (3-D) aspect of the code with a known theory. Again, very good agreement is found between DNS and LST results for the 3-D simulations, and this agreement indicates the disturbance amplitudes are sufficiently small that nonlinear interactions are negligible. The good agreement between DNS and LST results verifies that the 3-D aspect of the code is accurate.

1 Introduction

For the past century, numerous investigations have been conducted in an attempt to predict the transition from laminar to turbulent flow in boundary layers. Most of this effort stems from the independent early theoretical accomplishments of Orr (refs. 1 and 2) and Sommerfeld (ref. 3) at the turn of the 20th century. Their achievement, based on linearized disturbance equations, is a successful example of *classical hydrodynamic stability theory* and is referred to as the Orr-Sommerfeld equation. It was not until some 20 years later that Tollmien (ref. 4) was able to solve the Orr-Sommerfeld equation, and this solution led to the calculation of a critical Reynolds number for the onset of instability. On the same subject, Schlichting (ref. 5) computed amplification rates of disturbances in the boundary layer. Part of the first experimental confirmation of the theory was given by Schubauer and Skramstad (refs. 6 and 7), who used a vibrating ribbon to impress a disturbance into the boundary layer and hot wires (which were now available) to take measurements. With these contributions (and others) spanning some 40 years, theory and experiments now agreed on the initial growth of disturbances. Today, we have various mathematical and computational tools available to solve the Orr-Sommerfeld equation. From this equation, much is now understood concerning boundary-layer disturbances, more commonly referred to as the Tollmien-Schlichting (TS) waves.

Since its origination, stability theory has gained wide acceptance and is now a well-established tool in the research and engineering community. Furthermore, it is from stability theory that the first reasonably comprehensive method for predicting transition was derived, the e^N-method by Smith and Gamberoni (ref. 8) and Van Ingen[1]. However, the

[1] Van Ingen, J. L.: A Suggested Semi-Empirical Method for the Calculation of the Boundary-Layer Transition Region. Rep. no. VTH-74, University of Delft (The Netherlands), 1956.

method is semiempirical and thus requires some foreknowledge of the flow undergoing transition. The true physical problem involves disturbances that interact in a nonlinear manner in later stages of transition, and these disturbances are embedded in a growing boundary layer. It is apparent that a method, which accounts for nonparallel flow and nonlinear interactions, is necessary to predict transition. At present, such an all-encompassing method of transition prediction is beyond our grasp, but progress has been made in recent years.

In the last decade, much excitement has arisen because of the strides that have been made in theoretical developments for predicting stages of transition beyond the linear growth stage. Stemming in part from pioneering attempts at nonlinear theories by Benney and Lin (ref. 9) and Craik (ref. 10), Orszag and Patera (ref. 11) and Herbert (ref. 12) derived a theory, based on Floquét theory, which accounts for an experimentally observed three-dimensional (3-D) parametric instability. Although the governing equations are linearized and a local parallel flow assumption is made, remarkable agreement is obtained between predictions from this new theory and experimental results, in particular for the peak-valley splitting mode identified by Klebanoff, Tidstrom, and Sargent (ref. 13) and for the peak-valley alignment mode observed by Kachanov and Levchenko (ref. 14). These are examples of two distinct and different routes to transition that are discriminated based on the initial disturbance levels. Since its introduction in the early 1980's and subsequent verification throughout that decade, the theory for secondary instabilities is generally accepted and is now widely used by the research community as a tool to further understand and predict transition in boundary layers.

More recently, Herbert (ref. 15) and Bertolotti (ref. 16) have devised a nonlinear, nonparallel computational method based on the so-called "parabolized stability equations" (PSE's). The full benefits and limitations of this new theory are yet to be realized and are explored somewhat in this paper. Prior to development of this theory, the only approach to solve the nonparallel, nonlinear boundary-layer transition problem was by direct numerical simulation (DNS), although researchers have had some success with asymptotic methods to solve problems in the large Reynolds number limit (Smith (ref. 17) and Hall and Smith (ref. 18)). To date, most studies using DNS have been limited to the temporal formulation, in which a spatially periodic computational domain travels with the disturbance and the temporal evolution of the disturbance is computed. This enabled simulations into the later stages of transition (Zang and Hussaini (refs. 19 and 20) and Laurien and Kleiser (ref. 21)), and thus provided a data base of qualitative information that, however, lacks the physically realistic spatial representation. Spatial DNS provides needed quantitative information about transition. But with spatial DNS, obstacles exist that have prevented fully carrying out such a study. Among these are the realistic specification of inflow and outflow conditions and high demands on computational resources. Even with today's supercomputers, current resources are insufficient to fully simulate transition to turbulence in a boundary layer in a spatial setting. However, Rai and Moin (ref. 22) have demonstrated that the qualitative characteristics of the transition process can be captured with todays computers.

Yet, progress in spatial DNS has been made by, among others, Fasel, Rist, and Konzelmann (refs. 23 to 26) and Spalart (ref. 27) for boundary-layer flow and Danabasoglu, Biringen, and Streett (ref. 28) for channel flow. To date, results obtained from spatial DNS have been compared qualitatively and, with some success, quantitatively to results from linear stability theory (LST), secondary instability theory, and available experiments. For a more complete list of accomplishments in transition prediction through the use of DNS, refer to the recent review by Kleiser and Zang (ref. 29).

The goal of the present research effort is to introduce a spatial DNS approach that adequately handles outflow problems that can arise, that properly captures the flow physics, and that establishes a parametric understanding of DNS. The accomplishment of this goal would lead to potential benchmark solutions for use with future theories. To accomplish this goal, confidence in the numerical techniques must be established. In this initial study, results from simulations of boundary-layer flow over a flat plate are compared with those from LST and PSE theory.

Symbols

$A^o_{n,m}$	inflow amplitudes of forced disturbances
$\mathbf{B}$	LST matrix
C_i	coefficients for Runge-Kutta marching, $i = 1, 2, 3$
$\mathbf{C_i}$	matrix coefficients for LST, $i = 0, 1, 2, 3, 4$
$\widetilde{\mathbf{C}}_i$	transformed matrix coefficients for LST, $i = 0, 1, 2, 3, 4$

$\mathbf{D}$	collocation derivative operator
F	right-hand side of pressure equation
F_r	wave frequency
$f(\tilde{y})$	similarity dependent variable
G	right-hand side of eigenvector decomposition technique
$H(\mathbf{u})$	momentum equation operator
h_t	time-step size
h_x	streamwise step size
$\mathbf{I}_{\mathrm{NF}}$	modified influence matrix
$L(\mathbf{u})$	momentum equation operator
N_B	size of modified influence matrix
N_b	beginning of buffer domain
N_x, N_y, N_z	number of streamwise, wall-normal, and spanwise grid points
P	mean-flow pressure component
p	disturbance pressure component
$\tilde{p}$	instantaneous pressure
$\mathbf{Q}$	eigenvector matrix of $\mathbf{D}^2$-operator
$\mathbf{Q}^{-1}$	inverse of $\mathbf{Q}$-matrix
R_x	Reynolds number based on streamwise coordinate
R^*	Reynolds number based on local displacement thickness
R_o^*	Reynolds number based on inflow displacement thickness
s_j	attenuation function for buffer-domain technique
s_p	parameter for grid stretching normal to wall
T	period of disturbance, $T = 2\pi/\omega$
$T_n(\overline{y})$	Chebyshev polynomial of order n
Tr	matrix trace
t	time
U, V, W	mean-flow streamwise, wall-normal, and spanwise velocities
$\mathbf{U}$	mean-flow velocity vector, $\mathbf{U} = (U, V, W)$
U_∞	free-stream velocity
u, v, w	disturbance streamwise, wall-normal, and spanwise velocities
$\tilde{\mathbf{u}}$	instantaneous velocities, $\tilde{\mathbf{u}} = \mathbf{U} + \mathbf{u}$
$\mathbf{u}$	disturbance velocity vector, $\mathbf{u} = (u, v, w)$
$\mathbf{X}^T$	transpose of fourth-order penta-diagonal matrix
x, y, z	streamwise, wall-normal, and spanwise coordinate directions
$y_{\max}$	physical far-field boundary distance
$\tilde{y}$	similarity variable, $\tilde{y} = y\sqrt{R_x}/x$
$\overline{y}$	spectral domain variable, $\overline{y} \in [-1, 1]$
α, β	disturbance streamwise and spanwise wave numbers
Γ	computational domain
$\partial\Gamma$	computational boundary
δ^*	local displacement thickness
δ_o	boundary-layer thickness at inflow
δ_o^*	displacement thickness at inflow
$\mathbf{\Lambda}$	eigenvalue matrix of $\mathbf{D}^2$-operator
λ_x, λ_z	disturbance streamwise and spanwise wavelengths
ν	fluid kinematic viscosity
ξ	temporary variable, $\xi = dv/d\tilde{y}$
Φ	dependent variable for eigenvector decomposition technique
ψ	mean-flow stream function
$\wp$	pressure-like variable
Ω	disturbance normal vorticity
ω	disturbance frequency
∇	divergence operator
Subscripts:	
max	maximum
n	gradient normal to boundary
τ	tangential component
∞	free-stream conditions
Superscripts:	
m	Runge-Kutta time step
(m)	higher order derivatives

n	full-time-step quantities
o	with respect to inflow quantity
T	matrix transpose
(v)	fifth-order derivative
(vi)	sixth-order derivative
$*$	with respect to displacement thickness

Notation:

B-6	Bertolotti PSE with six modes
C-5	Chang PSE with five modes
DNS	direct numerical simulation
DL	DNS with LST inflow
DP	DNS with PSE inflow
LST	linear stability theory
PSE	parabolized stability equation
RK	Runge-Kutta
rms	root-mean-square
TS	Tollmien-Schlichting

A circumflex over a symbol indicates it is a series coefficient.

2 Governing Equations

The incompressible Navier-Stokes equations are solved in the domain shown in figure 1. The streamwise direction is x, the direction normal to the wall is y, and the spanwise direction is z. The corresponding instantaneous velocities are $\tilde{\mathbf{u}} = (\tilde{u}, \tilde{v}, \tilde{w})$ and the pressure is $\tilde{p}$. The momentum equations are given by

$$\tilde{\mathbf{u}}_t + (\tilde{\mathbf{u}} \cdot \nabla)\tilde{\mathbf{u}} = -\nabla\tilde{p} + \frac{1}{R_o^*}\nabla^2\tilde{\mathbf{u}} \tag{1}$$

and the continuity equation by

$$\nabla \cdot \tilde{\mathbf{u}} = 0 \tag{2}$$

where subscripts on the dependent variables denote partial derivatives with respect to that subscripted variable. The equations are nondimensionalized with respect to the free-stream velocity U_∞, the kinematic viscosity ν, and some length scale at the inflow (say, displacement thickness δ_o^*). A Reynolds number can then be defined as $R_o^* = U_\infty \delta_o^*/\nu$. The instantaneous velocities $\tilde{\mathbf{u}}$ and pressure $\tilde{p}$ may be decomposed into mean-flow components, $\mathbf{U} = (U, V, W)$ and P, and fluctuating components, $\mathbf{u} = (u, v, w)$ and p:

$$\tilde{\mathbf{u}}(\mathbf{x}, t) = \mathbf{U}(\mathbf{x}) + \mathbf{u}(\mathbf{x}, t) \quad \text{and} \quad \tilde{p}(\mathbf{x}, t) = P(\mathbf{x}) + p(\mathbf{x}, t) \tag{3}$$

where $\mathbf{x} = (x, y, z)$. Thus, the flow field is a composite of mean and unsteady solution components, which are determined and computed in the following manner.

2.1 Mean-Flow Component

The mean boundary-layer flow on a flat plate may be described by the boundary-layer equations, which are parabolic in the streamwise (x) direction. Although a marching algorithm may be used to solve the equations for the mean flow (U, V), the widely used Blasius similarity profile is employed for the present study. A detailed description and derivation of the mean-flow equations are provided in appendix A.

2.2 Disturbance Component

The disturbance, or fluctuating, components of equations (3) are determined by solving the form of the Navier-Stokes equations that results from our substituting equations (3) into equations (1) and (2) and subtracting out the mean-flow equations. These unsteady, nonlinear disturbance equations are

$$\mathbf{u}_t + (\mathbf{u} \cdot \nabla)\mathbf{u} + (\mathbf{U} \cdot \nabla)\mathbf{u} + (\mathbf{u} \cdot \nabla)\mathbf{U} = -\nabla p + \frac{1}{R_o^*}\nabla^2\mathbf{u} \tag{4}$$

and the continuity equation is

$$\nabla \cdot \mathbf{u} = 0 \tag{5}$$

with boundary conditions

$$\mathbf{u} = 0 \quad \text{at} \quad y = 0 \quad \text{and} \quad \mathbf{u} \to 0 \quad \text{as} \quad y \to \infty \tag{6}$$

Outflow conditions are provided by parabolizing the governing equations (4) over a small portion of the downstream computational domain. An illustration of this is shown in figure 1. This procedure, known as the buffer-domain technique, is described in a later section.

Various analytical and numerical techniques are now available to introduce a disturbance into the boundary layer. For example, Fasel, Rist, and Konzelmann (ref. 26) used time-periodic suction and blowing, while Kral and Fasel (ref. 30) used heater strips. An alternative form of disturbance forcing is to introduce a prescribed time-periodic function

at the inflow or the free-stream boundary. For the present study, the disturbance forcing takes the form of eigenfunctions imposed at the inflow boundary. Since the emphasis of this study is to verify the numerical techniques used in the simulations, a controlled input is required, which may be used by the DNS, LST, and PSE codes.

The inflow condition $\mathbf{u}_{\text{in}}$ is given by the mean flow and a disturbance-forcing function, or

$$\mathbf{u}_{\text{in}} = \mathbf{U}_o + \mathbf{u}^o \quad \text{at} \quad x = 0 \tag{7}$$

where $\mathbf{U}_o$ is the inflow mean component. For the present simulations, the disturbances take the form of a linear combination of individual functions:

$$\mathbf{u}^o = \sum_{m=-M}^{m=M} \sum_{n=-N}^{n=N} A^o_{n,m} \cdot \text{Re}\left[\hat{\mathbf{u}}^o_{n,m}(y) e^{i(m\beta z - n\omega t)}\right] \tag{8}$$

where $A^o_{n,m}$ represents the 2-D and 3-D disturbance amplitudes, which for the flat-plate boundary layer are the amplitudes of Tollmien-Schlichting waves, β is a spanwise wave number, and ω is the real disturbance frequency. Time periodicity is assumed, with the period $T = 2\pi/\omega$. Also, $\hat{\mathbf{u}}^o_{n,m}(y)$ represents the complex eigenfunctions either found from solving the Orr-Sommerfeld and Squire equations or obtained from a local approximation of the PSE, and the eigenfunctions are normalized by the maximum streamwise component. Descriptions of LST and PSE theory and their numerical solution procedures are given in appendixes B and C.

3 Numerical Methods

In this section, the following numerical techniques required for the spatial simulation are discussed: (1) discretization(s) in the streamwise, wall-normal, and spanwise directions; (2) time-splitting procedure, from which Poisson equations (2-D) or Helmholtz equations (3-D) for the pressure are obtained; (3) the eigenvector-decomposition method and the influence-matrix method, which are employed to solve for the pressure; (4) slip-velocity corrections, which are introduced because the pressure equation is inviscid to ensure that the tangential boundary conditions on velocity remain intact; and (5) buffer-domain technique, which is used to prevent wave reflections at the outflow.

3.1 Spatial Discretization(s)

3.1.1 Discretization in the streamwise direction. In the streamwise direction (x-direction), fourth-order central finite differences for the pressure equation and compact differences for the momentum equations are used on the computational domain of N_x discrete points. At boundary and near-boundary nodes, fourth-order differences are used. Although nonuniform grids have been implemented and tested, the present study involves the use of a uniform streamwise mesh. In this section, both differencing methods are discussed.

The objection to, or difficulty with, using higher order schemes comes from the required use of additional nodes to achieve the higher accuracy. For central differencing, complications may arise at or near a boundary, where insufficient nodes are available for the differencing. While approximations by forward or backward differences may be used, this may reduce the overall global order of the scheme or introduce numerical instabilities.

For the standard central, forward, or backward finite-difference approximations, the function of interest is expanded in a Taylor series as

$$f_{n+1} = f_n + h_x f'_n + \frac{h_x^2}{2} f''_n + \ldots + \frac{h_x^m}{m!} f_n^{(m)} + O(h_x^{m+1}) \tag{9}$$

where f_n is the function evaluated at node n; h_x is the step size, uniform for simplicity; and (m) denotes the higher order derivatives. Through expansion of neighboring nodes in similar series about node n and combination with equation (9), fourth-order central-difference approximations may be found for the first and second derivatives f'_n and f''_n:

$$f'_n = \frac{1}{12h_x}(f_{n-2} - 8f_{n-1} + 8f_{n+1} - f_{n+2}) + O(h_x^4) \tag{10}$$

$$f''_n = \frac{1}{12h_x^2}(-f_{n-2} + 16f_{n-1} - 30f_n + 16f_{n+1} - f_{n+2}) + O(h_x^4) \tag{11}$$

These approximations are used for the interior nodes (i.e., those nodes for which the derivative stencil does not extend beyond the boundary nodes). For boundary and near-boundary nodes, fourth-order forward and backward differences formed in a similar manner are used. An explicit form of these forward- and backward-difference relations is provided in appendix D.

As the order of the approximation increases, the required number of boundary and near-boundary relations and the corresponding required number of

nodes per derivative stencil increase. Therefore, to achieve higher accuracy without involving the use of additional neighboring nodes, compact differencing is introduced.

As originally suggested by Kreiss and Oliger (ref. 31) and later discussed for fluid dynamics problems by Hirsh (ref. 32), first and second derivatives for a compact difference may be approximated by

$$f'_n = \left(\frac{D_o}{1 + \frac{1}{6} h_x^2 D_+ D_-} \right) f_n \tag{12}$$

and

$$f''_n = \left(\frac{D_+ D_-}{1 + \frac{1}{12} h_x^2 D_+ D_-} \right) f_n \tag{13}$$

where

$$\left.\begin{aligned} D_o f_n &= \frac{1}{2h_x}(f_{n+1} - f_{n-1}) \\ D_+ f_n &= \frac{1}{h_x}(f_{n+1} - f_n) \\ D_- f_n &= \frac{1}{h_x}(f_n - f_{n-1}) \end{aligned}\right\} \tag{14}$$

Through multiplication of equations (12) and (13) by the respective denominators, relations for the derivatives may be found:

$$\frac{1}{6} f'_{n-1} + \frac{2}{3} f'_n + \frac{1}{6} f'_{n+1} = \frac{1}{2h_x}(f_{n+1} - f_{n-1}) \tag{15}$$

and

$$\frac{1}{12} f''_{n-1} + \frac{5}{6} f''_n + \frac{1}{12} f''_{n+1} = \frac{1}{h_x^2}(f_{n+1} - 2f_n + f_{n-1}) \tag{16}$$

These equations yield tridiagonal systems, provided appropriate boundary conditions are applied. The approximations are fourth-order accurate and can be solved efficiently by LU-decomposition with appropriate backward and forward substitutions.

To make an accuracy comparison between the compact-difference (eqs. (15) and (16)) and the central-difference (eqs. (10) and (11)) scheme, Taylor series expansions are employed. As Hirsh has shown, the truncation errors for the compact differences are

$$E(f'_n) = -\frac{1}{180} h_x^4 f^{(v)} \quad \text{and} \quad E(f''_n) = -\frac{1}{240} h_x^4 f^{(vi)} \tag{17}$$

while similar error analyses for the central differences yield

$$E(f'_n) = -\frac{1}{30} h_x^4 f^{(v)} \quad \text{and} \quad E(f''_n) = -\frac{1}{90} h_x^4 f^{(vi)} \tag{18}$$

Although both schemes are fourth-order accurate, the compact-difference scheme should lead to more accurate approximations as a result of having smaller coefficients on the truncation error.

As yet, no mention has been made about the boundary treatment for the compact-difference scheme. At the boundaries, Hirsh (ref. 32) used a one-sided fourth-order finite difference. Adam (ref. 33) suggested additional boundary relations that include near-boundary derivatives in the formulation; yet, the equations retain the tridiagonal nature. However, these relations are third-order accurate and indicate no additional benefits, compared with direct application of high-order one-sided differences. So, for the present compact-difference scheme, one-sided fourth-order finite-difference boundary conditions are used. (See appendix D.)

Concerning the boundary condition treatment, one might choose the second-order boundary conditions since a numerical instability could be generated, in particular, at the inflow with the use of higher order approximations. For the present incompressible spatial DNS, this problem was not encountered with fourth-order boundary conditions; but, in attempts to use fifth-order boundary conditions or a sixth-order compact-difference scheme, a numerical instability appeared. Recently, this numerical instability for the sixth-order methods has been resolved through an alternate boundary condition formulation by Carpenter, Gottlieb, and Abarbanel (ref. 34). This new fifth-order boundary treatment has enabled the use of a sixth-order compact-difference scheme. Although numerical difficulties surrounding the sixth-order schemes have been resolved, the remainder of this study involves the use of fourth-order techniques since additional computational expense arises solely from the higher order method. In a future study, a comparison of the fourth- and sixth-order techniques may be undertaken to determine if the accuracy gains with the sixth-order method outweigh the additional computational expense.

3.1.2 Discretization in the wall-normal direction. Normal to the wall (y-direction), Chebyshev series are used to approximate the disturbance at Gauss-Lobatto collocation points. A Chebyshev series is used since, as Gottlieb and Orszag (ref. 35) have shown, it provides good resolution in regions

of high gradients (e.g., near boundaries). Properties of Chebyshev series with collocation grids are given in Gottlieb, Hussaini, and Orszag (ref. 36). A detailed discussion of spectral method properties and their application is provided by Canuto, Hussaini, Quarteroni, and Zang (ref. 37). In the present paper, only a brief description of the necessary identities is provided.

The Gauss-Lobatto points for Chebyshev series are

$$\overline{y}_i = \cos(\pi i/\overline{N}_y) \quad (i = 0, 1, \cdots, \overline{N}_y) \tag{19}$$

where $\overline{N}_y$ is the number of domain intervals (or highest degree of Chebyshev polynomials in the series) and $N_y = \overline{N}_y + 1$ denotes the number of collocation points. Chebyshev polynomials are defined on the interval $[-1, 1]$ and are given by

$$T_n(\overline{y}) = \cos(n \cos^{-1} \overline{y}) \tag{20}$$

where n is the order of the Chebyshev polynomial T_n. A function $f(\overline{y})$ may be represented by a Chebyshev series at the Gauss-Lobatto points as

$$f(\overline{y}) = \sum_{n=0}^{\overline{N}_y} a_n T_n(\overline{y}) \tag{21}$$

where a_n represents the series coefficients. Derivatives of the function at collocation points may be represented by

$$\frac{df(\overline{y}_i)}{d\overline{y}} = \overline{\mathbf{D}}_{i,j} a_j \tag{22}$$

where repeated indices indicate summation. The derivative matrix $\overline{\mathbf{D}}$ is given by

$$\left.\begin{aligned} \overline{\mathbf{D}}_{i,j} &= \frac{c_i}{c_j} \frac{(-1)^{i+j}}{\overline{y}_i - \overline{y}_j} \qquad (i \neq j; i, j = 0, 1, \cdots, \overline{N}_y) \\ \overline{\mathbf{D}}_{j,j} &= -\frac{\overline{y}_j}{2(1 - \overline{y}_j^2)} \qquad (j = 1, 2, \cdots, \overline{N}_y - 1) \\ \overline{\mathbf{D}}_{0,0} &= -\frac{2\overline{N}_y^2 + 1}{6} = -\mathbf{D}_{\overline{N}_y, \overline{N}_y} \end{aligned}\right\} \tag{23}$$

where c_i and $c_j = 1$ for $i, j = 1, 2, \ldots, \overline{N}_y - 1$ and $c_0 = c_{\overline{N}_y} = 2$. Higher order derivatives are simply multiple powers of $\overline{D}$, or

$$\overline{\mathbf{D}}_p = \overline{\mathbf{D}}^p \tag{24}$$

where p is the derivative order.

Since the spectral interpolation function equation (20) is defined on $[-1, 1]$ and the physical problem of interest has a semi-infinite domain $[0, \infty]$ or a truncated domain $[0, y_{\max}]$, a transformation is employed. Studies of spectral methods and mapping tranformations in unbounded regions have been conducted by Boyd (ref. 38) and Grosch and Orszag (ref. 39). Here an algebraic mapping is used:

$$y = \frac{y_{\max} s_p (1 + \overline{y})}{2s_p + y_{\max}(1 - \overline{y})} \tag{25a}$$

or

$$\overline{y} = \frac{(2s_p + y_{\max})y - y_{\max} s_p}{y_{\max}(s_p + y)} \tag{25b}$$

where $y \in [0, y_{\max})$, $\overline{y} \in [-1, 1]$, $y_{\max}$ is the normal distance from the wall to the far-field boundary in the truncated domain, and s_p controls the grid stretching in the direction normal to the wall. As a result of the stretching, the normal derivatives in equations (23) and (24) are modified as follows:

$$\mathbf{D} = m\overline{\mathbf{D}} \quad \text{and} \quad \mathbf{D}^2 = m^2\overline{\mathbf{D}}^2 + mm'\overline{\mathbf{D}} \tag{26}$$

where the metric is defined as $m = d\overline{y}/dy$ and $m' = dm/d\overline{y}$.

3.1.3 Discretization in the spanwise direction. To simulate the evolution of 3-D disturbances, the governing equations must be discretized in the spanwise direction (z-direction) in addition to the streamwise and wall-normal directions. Some rationale in the choice of discretization must be used since, with this third dimension, the memory requirements and cpu cost for a simulation can quickly exceed current supercomputer capabilities. From boundary-layer experiments (refs. 13 and 14) it has been observed that a distinct periodic structure is evident in the spanwise direction. From this observation, spanwise periodicity is assumed, and this periodicity allows for Fourier series representations. With Fourier series, spectral accuracy is obtained in the spanwise direction and fast Fourier transforms (FFT's) or sine-cosine transforms may be used, either of which allows for the fast computing of derivatives.

In general, a function $f(x, y, z, t)$ is represented by a Fourier series expansion in the spanwise direction:

$$f(x, y, z, t) = \sum_{n=-N_z/2}^{(N_z/2)-1} \hat{f}_n(x, y, t) e^{in(2\pi/\lambda_z)z} \tag{27}$$

where N_z is the number of Fourier modes, $\lambda_z = 2\pi/\beta$ is the spanwise wavelength, and β is a specified spanwise wave number. To compute a derivative, equation (27) is first transformed to Fourier space by an FFT. The derivative is computed by

$$\frac{d\hat{f}_n}{dz} = i\hat{\beta}_n \hat{f}_n(x,y,t) \tag{28}$$

where $\hat{\beta}_n = n\beta$ and an inverse transform is used to return the computed derivative to physical space.

Although the full Fourier representation (eq. (27)) is correct if the spanwise direction is periodic, more cost-efficient derivatives are computed by cosine and sine expansions for the special, yet widely used, case of symmetry about $z = 0$ (e.g., wave triads and some secondary instability calculations). For the simulation problem, even functions (i.e., u, v, and p) are expanded with cosine series and odd functions (i.e., w) are expanded with sine series:

$$\{u,v,p\}(x,y,z,t) = \sum_{n=0}^{N_z} \{\hat{u}_n, \hat{v}_n, \hat{p}_n\}(x,y,t)\cos(n2\pi/\lambda_z z) \tag{29a}$$

and

$$w(x,y,z,t) = \sum_{n=0}^{N_z} \hat{w}_n(x,y,t)\sin(n2\pi/\lambda_z z) \tag{29b}$$

Equation (27) is used for a spanwise domain of a full wavelength (λ_z), while the use of the symmetry assumption with equations (29) permits computations on half the domain, or a half-wavelength ($\lambda_z/2$). This symmetry assumption decreases the computational (cpu and memory) requirements by approximately a factor of 2.

3.2 Time-Splitting Procedure

For the unsteady disturbance equations (4) to (6), a time-splitting procedure is used with implicit Crank-Nicolson differencing for normal diffusion terms and an explicit third-order Runge-Kutta method for all remaining terms. The Runge-Kutta (RK) scheme, introduced by Williamson (ref. 40), was implemented with the Crank-Nicolson method for Taylor-Couette flow calculations by Streett and Hussaini (ref. 41). This time-splitting procedure consists of three intermediate RK stages, each stage of the following form.

The pressure is omitted from the momentum equation (4) for the fractional RK stage, and this omission leads to

$$\frac{\mathbf{u}^\dagger - \mathbf{u}^m}{h_t^m} = C_1^m H^m(\mathbf{u}) + \frac{C_2^m}{R_o^*}\mathbf{D}^2(\mathbf{u}^\dagger + \mathbf{u}^m) \tag{30}$$

where

$$H^m(\mathbf{u}) = L^m(\mathbf{u}) + C_3^m H^{m-1}(\mathbf{u})$$

and

$$L(\mathbf{u}) = (\mathbf{U}\cdot\nabla)\mathbf{u} + (\mathbf{u}\cdot\nabla)\mathbf{U} + (\mathbf{u}\cdot\nabla)\mathbf{u} - \frac{1}{R_o^*}\nabla_{xz}^2\mathbf{u}$$

Here $\mathbf{u}^\dagger$ represents disturbance velocities at the intermediate RK stages, $\mathbf{u}^m$ represents velocities at previous RK stages ($m = 1, 2$, or 3), $\mathbf{u}^0$ represents velocities at the previous time step, $\nabla_{xz}^2 = \partial^2/\partial x^2 + \partial^2/\partial z^2$, and h_t is the time-step size. Recall that $\mathbf{D}$ is the derivative (eq. (26)). For a full RK stage, the momentum equations with the pressure are

$$\frac{\mathbf{u}^{m+1} - \mathbf{u}^m}{h_t^m} = C_1^m H^m(\mathbf{u}) + \frac{C_2^m}{R_o^*}\mathbf{D}^2(\mathbf{u}^{m+1} + \mathbf{u}^m) - \nabla p^{m+1} \tag{31}$$

Subtracting equation (30) from equation (31) leaves

$$\begin{aligned}\frac{\mathbf{u}^{m+1} - \mathbf{u}^\dagger}{h_t^m} &= \frac{C_2^m}{R_o^*}\mathbf{D}^2(\mathbf{u}^{m+1} - \mathbf{u}^\dagger) - \nabla p^{m+1} \\ &= -\nabla \wp^{m+1}\end{aligned} \tag{32}$$

where $\wp$ is an introduced pressure-like quantity. By taking the divergence of equation (32) and imposing zero divergence of the flow field at each RK stage ($m+1$), a pressure-like equation is obtained:

$$\nabla^2 \wp^{m+1} = \frac{1}{h_t^m}(\nabla\cdot\mathbf{u}^\dagger) \tag{33}$$

which is subject to homogeneous Neumann boundary conditions. (See ref. 41.) The solution procedure is as follows. The intermediate RK velocities $\mathbf{u}^\dagger$ are determined by solving equation (30). The pressure-like correction $\wp^{m+1}$ is found by solving equation (33). Then, the full RK stage velocities $\mathbf{u}^{m+1}$ are obtained from equation (32). Upon solution of the above system three consecutive times, full-time-step velocities $\mathbf{u}^{n+1}$ are determined. The RK coefficients and time steps are given by

$$\begin{bmatrix} C_1^1 & C_2^1 & C_3^1 \\ C_1^2 & C_2^2 & C_3^2 \\ C_1^3 & C_2^3 & C_3^3 \end{bmatrix} = \begin{bmatrix} 1 & \frac{1}{2} & 0 \\ \frac{9}{4} & \frac{1}{2} & -4 \\ \frac{32}{15} & \frac{1}{2} & -\frac{153}{32} \end{bmatrix} \tag{34a}$$

and

$$\begin{Bmatrix} h_t^1 \\ h_t^2 \\ h_t^3 \end{Bmatrix} = \begin{Bmatrix} \frac{1}{3}h_t \\ \frac{5}{12}h_t \\ \frac{1}{4}h_t \end{Bmatrix} \tag{34b}$$

where the sum of the three RK time stages equals the full time step h_t.

3.3 Eigenvector-Decomposition Method

To obtain the pressure-like correction $\wp$ for the 2-D and 3-D boundary-layer problems, solutions of Poisson equations for each time step are required. For 3-D simulations with spanwise periodicity assumed, the pressure correction is determined in transform space, for which the Fourier coefficients are solved. In transform space, the Poisson equations become Helmholtz equations. In order to solve the equations efficiently, a fast elliptic solver is required. For this purpose, the tensor-product, or eigenvector decomposition, approach is employed. Danabasoglu, Biringen, and Streett (ref. 28) used the eigenvector decomposition method for the 2-D channel problem. The present solver description is for the 3-D simulation problem.

The Helmholtz equations in transform space are given by

$$\nabla^2_{xy}\hat{\wp}_n - \hat{\beta}_n^2\hat{\wp}_n = \hat{F}_n \tag{35}$$

where $\hat{\beta}_n$ represents the spanwise derivative coefficients, or wave numbers, of equation (28). The term $\hat{F}_n$ represents the transform coefficients of F, where F is the right-hand side of equation (33), and $\hat{\wp}_n$ gives the transform coefficients of the desired solution, $\wp$.

With respect to matrix operations, (y, x) ordering is used below. Discretized in y and x, the Helmholtz equations become

$$\widetilde{\mathbf{D}}^2\hat{\wp}_n + \hat{\wp}_n\mathbf{X}^T - \hat{\beta}_n^2\hat{\wp}_n = \hat{F}_n \tag{36}$$

where $\widetilde{\mathbf{D}}^2$ is the Chebyshev-collocation operator in equation (26) modified to include boundary conditions, and $\mathbf{X}^T$ is the transpose of the streamwise central finite-difference operator, which for the present study is fourth-order accurate and leads to a pentadiagonal matrix. The matrix $\widetilde{\mathbf{D}}^2$ may be decomposed into

$$\widetilde{\mathbf{D}}^2 = \mathbf{Q}\mathbf{\Lambda}\mathbf{Q}^{-1} \tag{37}$$

where $\mathbf{\Lambda}$ is a diagonal matrix of eigenvalues and $\mathbf{Q}$ is the corresponding matrix of eigenvectors of $\widetilde{\mathbf{D}}^2$. A new dependent matrix is introduced and defined as

$$\Phi_n = \mathbf{Q}^{-1}\hat{\wp}_n \tag{38}$$

Substituting equations (37) and (38) into (36), one obtains

$$\mathbf{\Lambda}\Phi_n + \Phi_n\mathbf{X}^T - \hat{\beta}_n^2\Phi_n = \hat{G}_n \tag{39}$$

where $\hat{G}_n = \mathbf{Q}^{-1}\hat{F}_n$. Equation (39) is used to solve for $\mathbf{\Phi}_n$, which is then used in equation (38) to solve for $\hat{\wp}_n$. Since the coefficient matrix in equation (39) is pentadiagonal for fourth-order streamwise discretization, fast back substitutions result. The solution is then transformed through inversion to physical space. The derivative matrix $\mathbf{D}$, its inverse, and matrices $\mathbf{Q}$ and $\mathbf{Q}^{-1}$ are mesh-dependent matrices and need to be calculated only once; the same is true of the influence matrix, which is described in the next section. To reduce the computational cost, planes of the computational domain can be sent to the solver for vectorization. Sending the entire computational block may be done and leads to a more efficient solver, but the resulting memory requirements far outweigh the cost savings.

3.4 Influence-Matrix Method

Equations (30) to (33) are solved on a nonstaggered grid. An influence-matrix method is employed to solve for the pressure. Streett and Hussaini (ref. 41) used the method for the Taylor-Couette problem, and later Danabasoglu, Biringen, and Streett (ref. 28) used the method for the 2-D channel flow problem. Instead of solving a Poisson-Neumann problem, two Poisson-Dirichlet problems are solved.

The solution of the following Poisson-Dirichlet problem, which is the pressure-like equation, is sought:

$$\nabla^2\wp = F \quad \text{in} \quad \Gamma \tag{40a}$$

$$\wp_n = 0 \quad \text{on} \quad \partial\Gamma \tag{40b}$$

where Γ is the computational domain, $\partial\Gamma$ is the computational boundary, and $\wp_n$ indicates a derivative of the pressure-like quantity normal to the boundary $\partial\Gamma$. To accomplish this, a sequence of solutions to the following problem is first determined:

$$\nabla^2\wp^j = 0 \quad \text{in} \quad \Gamma \tag{41a}$$

$$\wp^j = \delta_{i,j} \quad \text{on} \quad \partial\Gamma \tag{41b}$$

for each discrete boundary point $\bar{x}_j$. The Dirac delta function $\delta_{i,j}$ is defined as $\delta_{i,j} = 1$ for $i = j$ and $\delta_{i,j} = 0$ for $i \neq j$. Upon computation of the vectors of normal gradients $\wp_n^j$ at all the boundary points, these vectors are then stored in columns to yield a matrix that is referred to as the influence matrix, or

$$\mathbf{I}_{\mathrm{NF}} = [\wp_n^1, \wp_n^2, \ldots, \wp_n^{N_B}] \tag{42}$$

where N_B is the number of boundary points.

The influence matrix, which is dense, is of order $N_B \times N_B$ for 2-D problems and of order $N_B \times N_B \times N_z$ for 3-D problems, and it is dependent on the computational mesh only. Since the matrix is dependent on the mesh, it need be calculated only once for a given geometry. However, the memory requirements for the influence matrix for a 3-D problem can quickly become overbearing and, thus, eliminate the possibility of performing simulations into later stages of transition. For example, this single matrix may easily require 70 Mbytes of memory in the early stages of transition of a standard 3-D problem with $N_z = 16$. However, since the Helmholtz equation (35) is solved in Fourier space, where the coefficients are independent of each other, this memory requirement can be alleviated with a small penalty of cpu time (fractions of a second). Through sequential reading of the planes $N_B \times N_B$ of the matrix from disk, the 70-Mbyte requirement dwindles to an acceptable 4-Mbyte size that is now independent of the spanwise discretization. In particular, for a Cray supercomputer, buffer in(out) commands can be used to read(write) data while the program continues to execute. Thus, the overhead cost is virtually negligible.

The composed influence matrix gives the residuals of $\wp$ as a result of the unit boundary condition influence, or

$$[\mathbf{I}_{NF}]\wp = \text{Residual} \tag{43}$$

The value of one boundary condition is temporarily relaxed so that the problem is not overspecified. This is done by setting one column of the influence matrix to zero, except for the boundary point of interest, which is set to unity. The corresponding residual in equation (43) is exactly zeroed.

The Poisson equation with Neumann boundary conditions is equivalent to the following solution of a Poisson problem and a Laplace problem (or Helmholtz problems) with Dirichlet boundary conditions. First, solve

$$\nabla^2 \wp^I = F \quad \text{in} \quad \Gamma \tag{44a}$$

$$\wp^I = 0 \quad \text{on} \quad \partial\Gamma \tag{44b}$$

Again, compute the gradients normal to the boundary $\wp_n^I$. This gives the influence of the right-hand side F on the boundary. Then, solve

$$\nabla^2 \wp^{II} = 0 \quad \text{in} \quad \Gamma \tag{45a}$$

subject to the boundary constraint

$$\wp^{II} = \mathbf{I}_{NF}^{-1} \cdot \wp_n^I \quad \text{on} \quad \partial\Gamma \tag{45b}$$

The final solution that satisfies the original problem and the boundary conditions is $\wp = \wp^I - \wp^{II}$.

Since the gradient, or boundary condition, at one discrete boundary point is relaxed in the influence-matrix formulation, the desired condition ($\wp_n = 0$) may not hold at that boundary point. In order to regain this boundary condition, the pressure problem (eqs. (44) and (45)) is resolved, but this time a nonzero constant (say 0.01) is added to the right-hand side of equations (44). A pressure correction $\overline{\wp}$ results. The composite solution satisfies the boundary conditions at all discrete nodes and consists, then, of a linear combination of $\wp$ and $\overline{\wp}$. This combination is found by satisfying the following two equations:

$$a_1 \wp_n + a_2 \overline{\wp}_n = 0 \quad \text{on} \quad \partial\Gamma_i \tag{46}$$

and

$$a_1 + a_2 = 1 \tag{47}$$

The final pressure correction $\wp^{m+1}$ is then given by

$$\wp^{m+1} = a_1 \wp + (1 - a_1)\overline{\wp} \quad \text{with} \quad a_1 = \overline{\wp}_n / (\overline{\wp}_n - \wp_n) \tag{48}$$

Upon solution for $\wp^{m+1}$, the full RK time-step velocities $\mathbf{u}^{m+1}$ are found via equation (32). As a note, the corner points are not included in the discretization and are used in the tangential slip-velocity correction only. The pressure at the corners is of minor significance and interpolations are sufficient to compute these pressures.

3.5 Slip-Velocity Corrections

The pressure-like correction equation (33) is an inviscid calculation and is well posed, provided that boundary conditions on the wall-normal component of velocity are enforced. At the end of each full RK time step, a nonzero tangential velocity component may arise at the computational boundary. This is referred to as a "slip velocity." This slip velocity may be made small in magnitude, compared with the RK step size h_t^m, by a proper choice of intermediate boundary conditions. The conditions used herein were described by Streett and Hussaini (ref. 41), based on the work of Fortin, Peyret, and Temam (ref. 42).

The slip velocities on the boundary for equation (32) are

$$\mathbf{u}_\tau^{m+1} = \mathbf{u}_\tau^* - h_t^m \, \nabla \wp_\tau^{m+1} \quad \text{on} \quad \partial\Gamma \tag{49}$$

where τ indicates a tangential component on the boundary $\partial\Gamma$. If $\mathbf{u}_\tau^* = 0$, then $\mathbf{u}_\tau^{m+1} = O(h_t^m)$. Expanding the gradient term of equation (49) into a Taylor series about $t = t^m$, one obtains

$$\nabla \wp_\tau^{m+1} = \nabla \wp_\tau^m + h_t^m (\nabla \wp_\tau^m)_t + O[(h_t^m)^2] \qquad (50)$$

Approximate the time derivative term of equation (50) by

$$(\nabla \wp_\tau^m)_t = \frac{\nabla \wp_\tau^m - \nabla \wp_\tau^{m-1}}{h_t^{m-1}} + O[(h_t^m)^2] \qquad (51)$$

and substitute equations (50) and (51) into equation (49). The slip velocity is reduced to $O[(h_t^m)^3]$, and the intermediate boundary conditions that result are given by

$$\mathbf{u}_\tau^* = \mathbf{u}_{BC} + h_t^m \left[\left(1 + \frac{h_t^m}{h_t^{m-1}} \right) \nabla \wp_\tau^m - \frac{h_t^m}{h_t^{m-1}} \nabla \wp_\tau^{m-1} \right] + O[(h_t^m)^3] \qquad (52)$$

where $\mathbf{u}_{BC} = 0$ for a rigid wall and $\mathbf{u}_{BC} = \mathbf{u}_o$ for an inflow condition or for a wall slot condition evaluated at the appropriate time in the RK stage.

3.6 Buffer-Domain Technique

The buffer-domain technique for effecting a nonreflecting outflow boundary treatment was introduced by Streett and Macaraeg (ref. 43). The technique is based on the recognition that, for incompressible flow, the ellipticity of the Navier-Stokes equations, and thus their potential for upstream feedback, comes from two sources: the viscous terms and the pressure field. Examination of earlier unsuccessful attempts at spatial simulations indicated that upstream influence occurs through the interaction of these two mechanisms; strong local velocity perturbations interact with the condition imposed at the outflow boundary to produce a pressure pulse that is immediately felt everywhere in the domain, especially at the inflow boundary. Therefore both mechanisms for ellipticity have to be treated. To deal with the first source of upstream influence, the streamwise viscous terms are smoothly reduced to zero through multiplication by an appropriate attenuation function in a "buffer region," which is appended to the end of the computational domain of interest. The viscous terms are unmodified in the domain of interest. To reduce the effect of pressure field ellipticity to acceptable levels, the source term of the pressure Poisson equation is multiplied by the attenuation function in the buffer domain. This is akin to introduction of an artificial compressibility in that region and locally decouples the pressure solution from the velocity computation in the time-splitting algorithm. Thus, in effect, the boundary-layer equations, which are parabolic and do not require an outflow condition, govern the solution at outflow. Finally, the advection terms are linearized about the imposed mean- or base-flow solution in order that the effective advection velocity, which governs the direction of disturbance propagation, is strictly positive at outflow even in the presence of large disturbances.

The attenuation function used in this work is similar to that of references 43 and 28:

$$s_j = \frac{1}{2} \left(1 + \tanh \left\{ 4 \left[1 - 2 \frac{(j - N_b)}{(N_x - N_b)} \right] \right\} \right) \qquad (53)$$

where N_b marks the beginning of the buffer domain and N_x marks the outflow boundary location. For illustration, the buffer-domain region is sketched in figure 1. As shown subsequently for the current problems, a buffer-domain length of about three streamwise wavelengths is adequate to provide a smooth enough attenuation function to avoid upstream influence.

The original buffer-domain implementation of reference 43 involved a fully spectral discretization, with a spectral multidomain being used in the streamwise direction as opposed to the high-order finite differences used herein and in reference 28. Thus, early testing of the buffer-domain method was done in an even more sensitive setting. Reference 43 shows a number of tests of the method in the context of channel flow, albeit they were produced with a code that had a slight error and produced a small kink in the wall vorticity distribution at outflow. Corrected, the fully spectral channel-flow simulation code produced results that agree with linear stability theory to five significant digits in disturbance growth rate. Additional unpublished test cases included simulations of Poiseuille-Benard flow, in which a strongly unstable wall temperature condition was imposed; the temperature equation was included in the solution scheme with the Boussinesq approximation. For this flow, the unstable thermal boundary conditions produced large recirculation cells, which in some cases had vertical disturbance velocities three times larger than the imposed Poiseuille base-flow centerline velocity. These recirculation cells were produced by growth of the instability (seeded by numerical roundoff error of the computer), a process that is known to possess a global, rather than convective, instability nature. The lack of upstream influence even in this extreme test was confirmed by comparison of vorticity

distributions across the channel for channel lengths that contained between 5 and 10 cells.

4 Results

For the present study, the numerical techniques employed for the spatial DNS code are systematically verified through comparison with the well-established LST and the more recently devised PSE theory. First, the present solutions from LST are compared with previously published results. Next, the results from the DNS with a 2-D disturbance forcing for both parallel and nonparallel mean flows are compared with the LST results. Third, DNS results from 2-D disturbance forcing are compared with the PSE predictions. The sensitivity of the inflow forcing is demonstrated. Finally, a 3-D simulation is conducted and discussed. The DNS results from wave-triad forcing are compared with LST results for small-amplitude disturbances. The authors extend their thanks to Gokhan Danabasoglu of the Department of Aerospace Engineering Sciences, University of Colorado at Boulder, for the use of his channel simulation code. Thanks also go to Fabio Bertolotti at the Institute for Computer Applications in Science and Engineering, Hampton, Virginia, for supplying his PSE results.

4.1 Solutions of LST

Although additional documentation of results derived from LST is arguably unnecessary in this era, for completeness and since a comparison of LST results with the DNS results is a part of this study, a brief independent code verification is performed for solving the Orr-Sommerfeld Squire problem, as described in appendix B.

Results of the Orr-Sommerfeld equation are well documented in the literature. Herein, comparisons are made with the results of Jordinson (ref. 44), who used a finite-difference approach. For a 2-D disturbance with Reynolds number R^* of 998 and frequency ω of 0.1122, Jordinson found the streamwise wave number α of $0.3086 - i0.0057$. If an a priori approximation of the eigenvalue is unknown, the spectral global method provides an initial estimate of the eigenvalue. With an initial guess (say, $0.3086 - i0.0057$), the local method is used to refine the eigenvalue. Convergence results for the local refinement method are shown in table 1. The present results are in good agreement with those of Jordinson.

Figure 2 shows the corresponding eigenfunctions for the above parameters. Good agreement occurs in this comparison of eigenvalue and eigenfunction, which demonstrates that sound results of LST are available for the DNS verification.

Table 1. Eigenvalues From LST

$[R^* = 998; \omega = 0.1122; y_{\max} = 75; sp = 10]$

N_y	α
32	$0.3086817 - i0.0055527$
36	$0.3086085 - i0.0057926$
40	$0.3086050 - i0.0056964$
44	$0.3085825 - i0.0057164$
48	$0.3085946 - i0.0057069$
52	$0.3084899 - i0.0057088$
56	$0.3085920 - i0.0057083$
60	$0.3085912 - i0.0057084$

4.2 Comparison of 2-D DNS and LST

In this section, the accuracy of the numerical methods used for the DNS calculations is tested for small-amplitude disturbances through comparison with LST results. Initially, a parallel mean flow is assumed. Although this is a physically unrealistic flow, it adequately mimics the LST assumptions and provides a good initial test case. A Reynolds number R_o^* of 900 and wave frequency F_r of $(\omega/R^*)\times 10^6 = 86$ at the inflow are chosen somewhat arbitrarily for the test case. In an attempt to determine the grid resolution requirements, computations are performed on a variety of grids from $40l_x \times 41$ to $100l_x \times 61$ (streamwise $\times$ wall-normal), where l_x refers to the number of TS streamwise wavelengths included in the domain and $40l_x$ denotes 40 grid points per wavelength. If, for example, $l_x = 3$, then the grid for $40l_x$ consists of 120 points in the streamwise direction. The results obtained from each grid are in agreement.

In the physical domain, the streamwise computational domain length is varied, depending on the number of TS wavelengths of information required. Normal to the wall, the domain length is fixed and extended from the wall to an upper truncation distance where the far-field boundary conditions are imposed. For parallel flow, the far-field boundary is varied from $y^* = 50$ to 100 (where $y^* = y/\delta_o^*$). A concern with the primitive variable formulation lies in the pressure calculation, which incidentally is avoided with the velocity-vorticity approach as a result of not having to solve for the pressure quantity. If the far-field boundary is an insufficient distance from the wall, an erroneous disturbance arises throughout the computational domain. This erroneous disturbance arises

as a result of enforcing the far-field boundary conditions too close to the wall. Similar errors arise with different numerical procedures. For example, disturbances in a boundary layer exponentially decay when approaching the far field. Using a shooting procedure, one can integrate the LST equations from the wall to the far-field boundary and match the computed solutions with asymptotically known solutions. If this matching is performed an insufficient distance from the wall, the computations will not converge to the correct solution. Similarly, the present error, which can arise from the far-field boundary conditions imposed an insufficient distance from the wall, leads to incorrect results.

From the computations with a parallel flow, a far-field boundary of $y^* = 50$ appears to be the minimum distance for an acceptable disturbance error. Normal to the wall, grid stretching is used for the boundary-layer computations in order to obtain meaningful results efficiently. Stretching factors s_p of 6 to 12 are chosen to provide a dense distribution of collocation points near the wall. (A smaller s_p clusters more points near the wall.) The number of time steps per TS wave period is varied from 200 to 1000 in order to arrive at a rational choice of the time-step size required. Visual agreement of the results is found for each of the time-step test cases. (This agreement translates to no more than 0.1-percent error.) Since the time-splitting procedure is third-order accurate, larger time-step sizes may be used (compared with those of a second-order Adam-Bashforth method). Computations of the present type involve numerous parameters (e.g., three-directional grid, far-field boundary location, streamwise domain length, and time-step size). To remove one of these parameters, a small time-step size is chosen. Hereafter, 320 time steps per period are used to maintain temporal accuracy through the nonlinear simulations.

As a first example, the streamwise direction consists of approximately 7 TS wavelengths with 40 grid points per wavelength. Further, these seven TS wavelengths are subdivided into a physical domain of four wavelengths and a buffer domain of three wavelengths. For the inflow, a 2-D disturbance described by equation (8) with amplitude $A^o_{1,0}$ of 0.1 percent is forced. The solutions of the Orr-Sommerfeld equation are used for the disturbance profile. The inflow forcing is turned on abruptly, and the results of the simulation after three and eight periods of forcing at the inflow boundary are compared with LST predictions in figure 3. The computed phase and amplitude for the streamwise u and wall-normal v disturbance velocity components with downstream distance are in agreement with the LST results. After eight periods of forcing, the leading wave has exited the computational domain without wave reflections. This is an indication that the buffer-domain technique is functional. From LST, the spatial growth rate is $\alpha_i = -0.004509$. Growth rates from the DNS are calculated by a simple central-difference approximation with the local maximum disturbance streamwise velocity component $u_{\max}$; this simple approximation yields the results and errors shown in table 2 for various grids. Very good agreement is found between LST and the present DNS results, compared with results from the crude differential method used to compute α_i.

Table 2. DNS Growth Rates From Simple Central-Difference Approximations

$N_x \times N_y$	$-\alpha_i$	Error[a], percent
$40l_x \times 41$	0.004438	1.57
$60l_x \times 41$	.004473	.80
$80l_x \times 41$	.004494	.33
$40l_x \times 61$	.004440	1.53
$60l_x \times 61$	.004473	.80
$80l_x \times 61$	.004494	.33

[a]Error based on comparison with LST growth rate of $\alpha_i = -0.004509$.

As demonstrated in figure 3, the buffer-domain technique has permitted waves to exit the outflow boundary without wave reflection. This is accomplished by specifying a buffer domain of three TS wavelengths. We determine this length by comparing the computed results using various buffer regions with LST. To demonstrate the effects of using a buffer domain of insufficient length, the previous DNS results of figure 3 are shown with erroneous results in figure 4. The incorrect results occur for a buffer-domain length of one TS wavelength. A number of buffer-domain parameter variations may be found that are adequate to implement the outflow conditions. The length of the buffer domain, the number of grid points, and the slope of the attenuation function are the important elements that may be varied. It is likely that having a small slope and a small change in slope of the function relative to the grid spacing is of the most importance; however, this postulation has not been confirmed by a parameter study. With the present attenuation function (eq. (53)), the slope is governed by the buffer-domain length and becomes smaller with length increase. Hence, the three-wavelength domain provides an adequate outflow region, while the one-wavelength domain does not.

Next, a nonparallel mean flow is used and the simulations are repeated. To ensure accuracy, 60 or more points per wavelength are used hereafter. For the nonparallel mean flow, computations with four periods of forcing are conducted. The streamwise u and wall-normal v velocity amplitudes of the disturbance, as computed by simulation and with LST, are shown in figure 5. The change in the length scale, as a result of the growing boundary layer, is evident and leads to an increase in growth rate and a shift in wavelength. Since $R_o^* = 900$ and $F_r = 86$ correspond to a growing mode near the lower branch of the neutral curve, increasing growth rates are expected with downstream propagation. This is consistent with the results in figure 5. Since LST neglects nonparallel effects, exact quantitative agreement is not expected here.

In summary, the numerical techniques used for spatial DNS were tested by a comparison with LST. This comparison was made because LST provides an adequate tool to verify the spatial simulation results for small-amplitude disturbances. Also, since LST is universally accepted and is a well-established theory, it lends credence to the DNS results. A parametric study was conducted to determine the effects of grid refinement and domain size and to determine an adequate time-step size. Furthermore, the outflow boundary treatment was successfully tested. A comparison with LST is limited in scope because of the underlying assumptions of the theory. Better insight into the flow physics of transition and a better understanding of the DNS numerics could be achieved if results from DNS were compared with a more complete theory or experiments.

4.3 Comparison of DNS and PSE Theory

Recently, a new theory (PSE) has emerged that accounts for boundary-layer growth and nonlinear disturbance interactions. In this section, the results from spatial DNS are compared with PSE theory predictions. First, the effects of inflow disturbance variations and grid refinement on the solutions of the DNS in the linear and nonlinear regime are discussed. Second, DNS results are compared with those of PSE theory. Inferences are drawn by comparing DNS results to the distorting mean flow results of PSE theory.

As with Bertolotti (ref. 16), calculations are made with an inflow Reynolds number R_o^* of 688.315, a frequency F_r of 86, and a 2-D disturbance forcing at the inflow with amplitude $A_{1,0}^o$ of 0.25 percent rms. The inflow corresponds to a streamwise location prior to branch I of the neutral curve, in a region of disturbance decay. With this inflow amplitude, the disturbance decays initially until branch I of the neutral curve is reached, where the wave then begins to grow. The disturbance amplitude grows through the region of instability. Farther downstream, after passing branch II of the neutral curve and entering the region of stability, the wave saturates, or decays. The task at hand is to accurately predict the growth and decay of this evolving wave.

4.3.1 DNS parameter variation. How disturbances are ingested into the boundary layer and the effects of this ingestion are topics of the study of "receptivity." (See Reshotko, ref. 45.) For the present study, the presence of an ingested disturbance is assumed, and the evolution of that disturbance with downstream distance is computed; however, it is of utmost importance to know and understand how small changes in the disturbance (amplitude or profile) affect the computed downstream evolution. It is generally accepted that small differences in disturbance amplitudes at ingestion into the boundary layer lead to varying locations of transition. Although these differences in the disturbance may be small at the inflow, they may amplify downstream.

To demonstrate the sensitivity of spatial DNS to inflow disturbance variations, two specific DNS computations are performed with inflows from LST and PSE approximations of the Navier-Stokes equations. Hereafter, these two simulation cases are referred to as DL and DP, respectively. Since PSE theory is an integral method, its inflow condition must be prescribed by some local approximation, such as was prescribed and used by Chang, Malik, Erlebacher, and Hussaini (ref. 46). The DNS computations are performed on five different grid and inflow variations and are forced for approximately 28 to 31 TS periods. These five cases are shown in table 3. These test cases give a variation in inflow, grid resolution, and wall-normal domain length.

Table 3. Direct Numerical Simulation Test Cases

Case	$N_x \times N_y$	Far field $y_{\max}^*$
DL-41	$60l_x \times 41$	75
DP-41	$60l_x \times 41$	75
DL-61	$60l_x \times 61$	75
DP-61	$80l_x \times 61$	100
DP-81	$60l_x \times 81$	75

Figure 6 shows the maximum streamwise amplitudes of the Tollmien-Schlichting (fundamental)

wave u_1, the mean-flow distortion u_0, and the first harmonic u_2 with downstream distance for LST and PSE inflows on the grid $60l_x \times 41$ (DL-41 and DP-41). In the regions of small amplitudes (linear), the results from both inflows are in good agreement. Farther downstream, the wave amplitudes increase to levels where nonlinearities are significant. A slight variation in the results for the two inflows arises; at the saturation of the fundamental wave, the difference between the two wave amplitudes is 2.5 percent. The streamwise u and wall-normal v velocity components for the LST and PSE inflow profiles are given in figure 7. The LST profile is almost indistinguishable from the PSE profile. One might initially overlook the infinitesimal differences, but these differences are clearly amplified downstream (fig. 6). This suggests that the evolution of a disturbance is very sensitive to small changes in that disturbance. Careful consideration of the disturbance inputs is of utmost importance when any computed results are compared with those of theory or experiments; otherwise, improper conclusions could result.

For the next comparison, the computation grid is refined to $60l_x \times 61$ (DL-61) and $80l_x \times 61$ (DP-61), with corresponding far-field boundaries of $y^*_{\max} = 75$ and $y^*_{\max} = 100$. The resulting streamwise amplitudes of the fundamental wave u_1, the mean-flow distortion u_0, and the first harmonic u_2 are shown with downstream distance in figure 8. Similar to the previous results (fig. 6), the amplitudes agree in the linear regime and a maximum discrepancy appears near saturation. Altering the far-field distance and refining the streamwise grid leads to insignificant variation in visual comparisons of the results. However, refining the normal grid from 41 to 61 collocation points leads to larger saturation amplitudes. This effect indicates that the normal grid may not be adequate. To obtain a grid-resolved solution, a final test case (DP-81) is computed for 81 collocation points with a PSE inflow. Results obtained on the various grids with a PSE inflow are shown in figure 9. The results indicate that a grid-resolved, or nearly grid-resolved, solution has been attained for the inflow disturbance considered. Also, note that a coarse grid leads to an underprediction of the saturation amplitudes for the fundamental wave, the mean-flow distortion, and the first harmonic.

To obtain the results shown in figure 9, a buffer domain of three TS wavelengths and 320 time steps per period is used. For the DP-81 case, the computations are restarted and permitted to continue until the leading wave front has exited the outflow boundary. This successfully demonstrates that the buffer-domain technique is functional for the nonlinear calculations. Finally, the computations are restarted using 416 time steps per period to determine if the results are time accurate. Visual comparisons of these results with those of figure 9 reveal no differences with the use of different time-step sizes. So 320 time steps per period are sufficient for the present test problem.

4.3.2 Results of DNS and PSE theory. In this section, the nonlinear spatial simulation results are compared with PSE calculations of Chang et al. (ref. 46) and Bertolotti (ref. 16). With the approach of Chang et al., a parametric study was conducted. It was determined that 100 points normal to the wall, a normal distance of $100\delta_o$, and 5 modes of the series given by equation (C1) lead to sufficiently accurate results for the present test problem. Any further refinement of the PSE grid or number of series modes leads to no visible change in the results. The streamwise step size was chosen from a comparison with a method of multiple-scales solution for a linear disturbance evolution. For appropriate step sizes good visual agreement of the results was found. The results of Bertolotti were obtained with six modes of the series from equation (C1). Hereafter, the Chang et al. and Bertolotti PSE cases are referred to as C-5 and B-6, respectively. Bear in mind that questions concerning PSE parameterization have not yet been fully answered. This is illustrated in the comparison of the C-5 and B-6 results, shown in figure 10. The streamwise amplitudes of the fundamental wave u_1, the mean-flow distortion u_0, and the first harmonic u_2 are shown with downstream distance. Good agreement of the two PSE results is found for the fundamental-wave amplitude in both the linear and nonlinear regimes, except for a small discrepancy in the saturation amplitude, which may be attributed to small differences in the inflow disturbance (figs. 6 and 8). However, a significant unexplained difference in the C-5 and B-6 mean-flow distortion quantities does appear. Similar to the DNS results (fig. 9), the C-5 results capture early evidence of the first harmonic between $R^* = 690$ and 900 (barely visible), while the B-6 results do not. With these differences in the PSE results noted, the converged DNS results (DP-81) are compared with the C-5 PSE results below. The PSE results of Bertolotti have been compared with DNS results in less detail than that of the present paper. (See ref. 15.) Good agreement was indicated by the Bertolotti comparison. Unlike the present study, wherein the same disturbance amplitudes and profiles are used, the Bertolotti comparison involved a matching of the disturbance amplitudes at some downstream location.

This C-5 case was selected and compared with the DP-81 results since it is the most controlled comparison: both calculations are forced with the same inflow disturbance. In figure 11, maximum streamwise amplitudes of the fundamental wave, the mean-flow distortion, and the first harmonic with downstream distance from DP-81 are compared with the C-5 results. Results for both the fundamental wave and the first harmonic are in good quantitative agreement throughout the linear and nonlinear regions, while some discrepancy occurs with the mean-flow distortion quantity in the nonlinear region. It may be advantageous to view this comparison on a logarithmic scale. (See fig. 12.) A comparison of this type suggests that results for the fundamental wave, the first harmonic, and the mean-flow distortion are in better agreement than is shown in figure 11. Also, the early evidence of the first harmonic between $R^* = 690$ and 900 is visually drawn out. It is apparent that finite-amplitude differences are suppressed while small differences in near-zero amplitudes are exaggerated as a result of the logarithmic scaling.

To further examine the DP-81 and C-5 results, disturbance profiles at two streamwise locations are presented in figures 13 to 16. Figures 13 and 14 show streamwise components at streamwise locations corresponding to local Reynolds numbers of $R^* = 1413$ and 1519, respectively. Figures 15 and 16 show wall-normal components at the same respective streamwise locations. As shown in figure 11, the first downstream location is midway through the calculation, where the mean-flow distortion has a sudden rise, and the second is near the fundamental-wave saturation. The pictured mean-flow distortion, fundamental wave, and first and second harmonic profiles predicted by DP-81 and C-5 are in good qualitative as well as quantitative agreement, even in regions of high gradients. As before, the exception lies in the mean-flow distortion quantity. The disturbance profiles of the streamwise components reveal that the DNS results agree well with the PSE results in regions of positive influence on the mean flow, while in regions of negative influence PSE theory predicts stronger distortions than does DNS. From figures 15 and 16, it is apparent that the wall-normal component of the mean-flow distortion computed by DP-81 is in agreement with the C-5 results near the wall, with the discrepancy increasing with distance from the wall. Most likely this discrepancy in the results is due to homogeneous Neumann conditions imposed in the far-field wall-normal component of the mean-flow distortion for PSE theory. Unlike the DNS approach, this approach leads to a nonzero wall-normal mean-flow component in the far field. As a result, the mean flow varies from the Blasius (mean) flow. This variation is shown in figure 17 by a comparison of results from the far-field Blasius solution with those from the PSE solution. The maximum difference in the mean flows occurs near the location of wave saturation.

As a final test, a simulation was repeated to determine the effects of Neumann far-field boundary conditions for the wall-normal component. For computational efficiency, the DP-61 case was used since the results appear sufficiently converged with 61 collocation points. (See fig. 9.) The results are shown in figure 18 along with the previous DP-61 and C-5 results. Changing the far-field boundary conditions results in no apparent variation in the fundamental-wave and the first harmonic results; however, the Neumann boundary condition affects the mean-flow distortion quantity slightly. Larger amplitudes of the mean-flow distortion result. The streamwise and wall-normal disturbance components for the DP-61 case with the Neumann far-field condition are given with the C-5 results in figures 19 to 22. These results correspond to $R^* = 1413$ and 1519. A careful comparison of the present profiles with the previous results (figs. 13 to 16), which have homogeneous Dirichlet far-field boundary conditions, reveals that better agreement between results from DNS and from PSE theory is found. Most significantly, the streamwise mean-flow distortion profiles with the Neumann boundary condition are in better agreement. Only slightly better agreement is achieved for the wall-normal mean-flow distortion profiles. It appears the PSE theory with the Neumann boundary condition has a strong effect on the mean-flow distortion and only a mild to negligible effect on the fundamental wave and the harmonics.

It is important to understand the differences in the DNS and PSE theory numerical methods to properly draw conclusions from the above comparisons. For the PSE theory approach, the disturbance is represented by a Fourier series, as described in appendix C. The equations are solved in coefficient space, where the dependent variables are the Fourier coefficients. Boundary conditions are imposed on each coefficient independently. For the zero-order coefficient (mean-flow distortion), the boundary-layer equations result; thus, the natural far-field boundary condition is a homogeneous Neumann condition on the wall-normal velocity component. For the fundamental wave and the harmonics, the homogeneous Dirichlet boundary conditions are the natural physical choice in the far field. For the DNS approach, the full-disturbance equations are solved and boundary conditions are imposed on the disturbance. A physically

realizable assumption is that the disturbances vanish in the far field, or free stream; thus, homogeneous Dirichlet boundary conditions on the disturbance are a "good" choice. When the DNS results are compared with the PSE theory results, differences should appear as a result of the different boundary conditions used. It is apparent that these differences are small and become most apparent in the mean-flow distortion quantities. Some DNS results were obtained with the Neumann boundary conditions used in the far field and are given with PSE theory results in figures 18 to 22. Again differences in the results are found. Evidently, significant differences remain in the boundary condition treatment even though both approaches use Neumann conditions. For the DNS case, a Neumann disturbance boundary condition is enforced, while for PSE theory, a Neumann mean-flow distortion component is enforced. This variation suggests that the flow may exit the far-field boundary in the DNS approach with nonzero velocities in the fundamental wave and the harmonics, while this cannot happen when the PSE theory is used. Basically, this difference suggests that the DNS results will not be identical to the PSE theory results.

Another possible explanation for the small discrepancy in the comparison of DNS with PSE theory is that as the disturbance grows and reaches finite amplitudes, an induced pressure gradient arises, which can be calculated by DNS. The PSE theory approach assumes negligible streamwise gradients, and the boundary-layer equations result for the mean-flow component; thus, PSE theory cannot account for the existence of the induced streamwise pressure gradient. This explanation to the discrepancy is under consideration and may be explored further.

4.4 Comparison of 3-D DNS and LST

To demonstrate the extension to allow for 3-D disturbances with a Fourier series (eqs. (27) and (29)) used in the spanwise direction, a final comparison is made between 3-D spatial DNS results and LST results for the parallel boundary layer. As in section 4.2, an inflow Reynolds number R_o^* of 900 and a wave frequency F_r of 86 are used. Computations are performed on a mesh $60l_x \times 41 \times 5$ (streamwise $\times$ wall-normal $\times$ spanwise) involving cosine-sine transforms. In the streamwise direction, the computational domain is six TS wavelengths long (three physical and three buffer), and each time period is divided into 320 time steps. At the inflow, a 2-D fundamental wave with amplitude $A_{1,0}^o$ of 0.01 percent and a pair of oblique waves each with amplitude $A_{1,\pm1}^o$ of 0.01 percent and spanwise wavelength λ_z of 20π are introduced. The results at spanwise locations of $z = 0$ and $z = \lambda_z/4$ after four TS periods of wave-triad forcing are given with LST results in figures 23 and 24. Good agreement is found for the small amplitudes considered. As a result of the good agreement between the DNS results and the LST results, one can conclude that the disturbance amplitudes are sufficiently small that nonlinear interactions are negligible.

5 Conclusions and Future Directions

In the present paper, a spatial direct numerical simulation (DNS) approach has been introduced for two- and three-dimensional (2-D and 3-D) boundary-layer transition problems. The numerical techniques have been tested by comparison of DNS results with results from the linear stability theory (LST) and from the newly developed parabolized stability equation (PSE) theory. Results of the present study are as follows:

1. Resulting wave amplitudes and phase from the DNS are in very good agreement with those from LST for 2-D and 3-D small-amplitude disturbances.

2. The influence and effect of small differences at the inflow have been demonstrated using LST and PSE theory profiles at the inflow. Even very small differences in amplitude or profile become amplified downstream.

3. In the comparison of DNS results with those of PSE theory, good overall quantitative agreement is found in the amplitudes and profiles. Questions of boundary condition treatment have arisen. A difference in the far-field boundary condition treatment for the PSE theory is identified and likely leads to the differing mean-flow distortion quantities. For transition prediction, where integral quantities are of importance, the PSE theory is likely to be a useful tool for the engineer.

Simulation studies of transition on swept wings, large-amplitude wave-wave interactions, 3-D suction and blowing for generating streamwise vortices, and subharmonic forced transition are all underway. Further detailed comparisons of PSE theory with spatial DNS for 3-D transitioning flows are also in progress. All these ongoing studies are directed toward quantifying transitional flows, which previously could only be solved for qualitative information.

NASA Langley Research Center
Hampton, VA 23665-5225
June 2, 1992

Appendix A

Mean-Flow Equations

For a laminar boundary layer, an order of magnitude analysis yields the importance of each term in the Navier-Stokes equations. Prandtl (ref. 47) obtained the first estimate by neglecting terms of order $1/R_x^2$ and higher. This led to the now-famous boundary-layer equations. For a 2-D, incompressible flow, these are

$$\frac{\partial U}{\partial x} + \frac{\partial V}{\partial y} = 0 \tag{A1}$$

$$U\frac{\partial U}{\partial x} + V\frac{\partial U}{\partial y} = -\frac{\partial P}{\partial x} + \frac{1}{R_x}\frac{\partial^2 U}{\partial y^2} = 0 \tag{A2}$$

subject to boundary conditions

$$U(x,0) = V(x,0) = 0 \quad \text{and} \quad U(x,\infty) = U_\infty(x) = 0 \tag{A3}$$

The first significant observation by Prandtl was that the normal pressure gradient is negligible and the pressure is a known function of x, which is assumed to be impressed on the boundary layer by the inviscid outer flow. The second item of importance is that second derivatives in x have been lost in the boundary-layer approximation, the result being parabolic equations in x. The equations may readily be solved computationally through use of a marching algorithm with x as the marching variable.

One of the most famous and widely used solutions to the boundary-layer equations (A1) to (A3) is the flat-plate similarity solution obtained by one of Prandtl's students, Blasius (ref. 48). For a parallel free-stream flow over a flat plate, the free-stream velocity U_∞ is constant. A stream function is defined in terms of a similarity parameter $\tilde{y}$ by

$$\psi = (\nu U_\infty x)^{1/2} f(\tilde{y}) \tag{A4}$$

where $\tilde{y} = \frac{y}{x} R_x^{1/2}$. Corresponding velocities are defined by

$$U = \frac{\partial \psi}{\partial y} \quad \text{and} \quad V = -\frac{\partial \psi}{\partial x} \tag{A5}$$

By substituting the velocities into the boundary-layer equations, one arrives at the following equation for the similarity profile:

$$f'''(\tilde{y}) + \frac{1}{2} f(\tilde{y}) f''(\tilde{y}) = 0 \tag{A6}$$

with boundary conditions from equations (A3), or

$$f(0) = f'(0) = 0 \quad \text{and} \quad f''(\tilde{y} \to \infty) \to 1 \tag{A7}$$

where a prime indicates $d/d\tilde{y}$. After equations (A6) and (A7) are solved, the resulting mean velocity profile components for the boundary layer are determined from equations (A5) and are given by

$$U = f'(\tilde{y}) \quad \text{and} \quad V = \frac{1}{2} R_x^{-1/2} \left[\tilde{y} f'(\tilde{y}) - f\right] \tag{A8}$$

Moreover, the displacement thickness δ^* may be computed and is given by

$$\delta^* = \int_0^{y\to\infty} (1 - U)\, dy = \frac{x}{R_x^{1/2}} \int_0^\infty (1 - f')\, d\tilde{y}$$

$$= \frac{x}{R_x^{1/2}} \lim_{\tilde{y}\to\infty} (\tilde{y} - f) = 1.7207678 \frac{x}{R_x^{1/2}} \tag{A9a}$$

or

$$\frac{\delta^*}{x} = 1.7207678 R_x^{-1/2} \tag{A9b}$$

A Reynolds number based on this local length scale may be defined as $R^* = U_\infty \delta^* / \nu$. With equations (A9), the mean flow (eqs. (A8)) can be consistently determined on the DNS mesh so that DNS result differences due to mean-flow variations are prevented.

Although the parabolic boundary-layer equations (A1) and (A2), which describe the mean flow, can be solved computationally by a marching algorithm, it is more convenient to use the similarity formulation equation (A4) and numerically solve the ordinary differential equation (A6). For the present problem, a fifth-order, fixed-step Runge-Kutta method described by Luther (ref. 49) is employed. The solutions are then retained on the computational mesh.

Appendix B

Linear Stability Theory

Governing Equations

The well-celebrated Orr-Sommerfeld (refs. 1 and 2) and Squire (ref. 50) equations have led to a better understanding of the linear region of transition. These equations are derived from a linearization of the Navier-Stokes equations (1) and (2). In terms of the normal velocity, the Orr-Sommerfeld equation is given by

$$\left(\frac{1}{R^*}\nabla^2 - U\frac{\partial}{\partial x} - \frac{\partial}{\partial t}\right)\nabla^2 v - \frac{d^2U}{d\tilde{y}^2}\frac{\partial v}{\partial x} = 0 \qquad \text{(B1)}$$

with boundary conditions

$$v, \frac{\partial v}{\partial \tilde{y}} = 0 \quad \text{at} \quad \tilde{y} = 0 \quad \text{and} \quad v, \frac{\partial v}{\partial \tilde{y}} \to 0 \quad \text{as} \quad \tilde{y} \to \infty \qquad \text{(B2)}$$

For 3-D disturbances, the equation for normal vorticity Ω, referred to as the Squire equation, is required in addition to the Orr-Sommerfeld equation. The Squire equation is

$$\left(\frac{1}{R^*}\nabla^2 - U\frac{\partial}{\partial x} - \frac{\partial}{\partial t}\right)\Omega - \frac{dU}{d\tilde{y}}\frac{\partial v}{\partial z} = 0 \qquad \text{(B3)}$$

with boundary conditions

$$\Omega = 0 \quad \text{at} \quad \tilde{y} = 0 \quad \text{and} \quad \Omega \to 0 \quad \text{as} \quad \tilde{y} \to \infty \qquad \text{(B4)}$$

Numerical Methods

For the present study, solutions of the LST equations (B1) to (B4) are required for an inflow condition. A global method is outlined to determine the discrete spectrum of interest, and a local method is presented that may be used to track eigenvalues and corresponding eigenvectors efficiently.

Both 2-D and 3-D disturbances are assumed to be travelling waves. A normal-mode form of solution is assumed and is given by

$$\{v, \Omega\} = \{\hat{v}, \widehat{\Omega}\}(\tilde{y})e^{i(\alpha x + \beta z - \omega t)} + \text{Complex conjugate} \qquad \text{(B5)}$$

where $\{\hat{v}, \widehat{\Omega}\}$ are the complex eigenvectors, ω is the real frequency, β is the spanwise wave number, and $\alpha = \alpha_r + i\alpha_i$ is the complex streamwise wave number. In stability theory, α_i gives a measure of the disturbance growth, or decay. The streamwise wavelength is defined by $\lambda_x = 2\pi/\alpha_r$. For 3-D instabilities, the spanwise wavelength is defined by $\lambda_z = 2\pi/\beta$.

Substituting the normal-mode form equation (B5) into equations (B1) to (B4) yields

$$\hat{v}'''' + a(\tilde{y})\hat{v}'' + b(\tilde{y})\hat{v} = 0 \qquad \text{(B6)}$$

$$\widehat{\Omega}'' + c(\tilde{y})\widehat{\Omega} + d(\tilde{y})\hat{v} = 0 \qquad \text{(B7)}$$

where

$$a(\tilde{y}) = -2(\alpha^2 + \beta^2) - iR[\alpha U_o(\tilde{y}) - \omega]$$

$$b(\tilde{y}) = (\alpha^2 + \beta^2)^2 + iR(\alpha^2 + \beta^2)[\alpha U_o(\tilde{y}) - \omega] + iR\alpha U_o''(\tilde{y})$$

$$c(\tilde{y}) = -(\alpha^2 + \beta^2) - iR[\alpha U_o(\tilde{y}) - \omega]$$

$$d(\tilde{y}) = -iR\beta U_o'(\tilde{y})$$

with boundary conditions

$$\hat{v}, \hat{v}', \widehat{\Omega} = 0 \quad \text{at} \quad \tilde{y} = 0 \quad \text{and} \quad \hat{v}, \hat{v}', \widehat{\Omega} \to 0 \quad \text{as} \quad \tilde{y} \to \infty \qquad \text{(B8)}$$

where a prime indicates $d/d\tilde{y}$ and $R = R_x^{1/2}$.

By introducing a temporary dependent variable $\xi = v'$, the derivative boundary conditions are removed. Substituting the derivative matrices (eqs. (26)), the Chebyshev series, and the temporary variable into equations (B6) to (B8) leads to

$$\xi_j - D_{i,j}v_j = 0 \quad \text{with} \quad \xi_N = 0 \qquad \text{(B9)}$$

and

$$(D^3_{i,j} + D_{i,j}a_j)\xi_j + b_j v_j = 0 \quad \text{with} \quad v_0 = v_N = \xi_0 = 0 \qquad \text{(B10)}$$

$$(D^2_{i,j} + c_j)\Omega_j + d_j v_j = 0 \quad \text{with} \quad \Omega_0 = \Omega_N = 0 \qquad \text{(B11)}$$

where

$$a_j = -[2(\alpha^2 + \beta^2) + iR(\alpha U_j - \omega)]\mathbf{I}$$

$$b_j = [(\alpha^2 + \beta^2)^2 + i\alpha R U_j'' + iR(\alpha^2 + \beta^2)(\alpha U_j - \omega)]\mathbf{I}$$

$$c_j = -[2(\alpha^2 + \beta^2) + iR(\alpha U_j - \omega)]\mathbf{I}$$

$$d_j = -(i\beta R U_j')\mathbf{I}$$

and $\mathbf{I}$ is the identity matrix.

The spatial stability of the boundary layer is of interest. The Reynolds number R, frequency ω, and spanwise wave number β are specified, and the complex streamwise wave number α is the eigenvalue.

Eliminating the dependent variable ξ and combining equations (B9) to (B11) results in the following matrix eigenvalue problem:

$$\mathbf{B}(\alpha)\{v_n, \Omega_n\}^T = 0 \tag{B12a}$$

where v_n and Ω_n are the coefficients of the series, or discrete functional values of the normal velocity and vorticity at the Gauss-Lobatto points, and

$$\mathbf{B}(\alpha) = \mathbf{C}_4\alpha^4 + \mathbf{C}_3\alpha^3 + \mathbf{C}_2\alpha^2 + \mathbf{C}_1\alpha + \mathbf{C}_0 \tag{B12b}$$

The matrix coefficients $\mathbf{C}_i$ are complex square matrices of order N for 2-D instabilities and of order $2N$ for 3-D instabilities. Matrices $\mathbf{C}_4, \mathbf{C}_3, \mathbf{C}_2$, and $\mathbf{C}_1$ are singular. The eigenvalue problem is nonlinear and of order four in the eigenvalue α. Various methods are available to solve such problems. Four approaches are given in some detail by Joslin (ref. 51). Herein, a global and a local method are used to generate an inflow disturbance forcing for the simulations and are described next.

Global Method

A global method gives the discrete spectrum of eigenvalues without a priori knowledge of the value. A method referred to as the linear companion matrix method was given by Gohberg, Lancaster, and Rodman (ref. 52). The method has been applied to the 2-D Orr-Sommerfeld problem with a flat-plate boundary layer by Bridges and Morris (ref. 53), among others.

The linear companion matrix method is a linearization of the nonlinear problem. An algebraic eigenvalue transformation $\lambda = 1/(\alpha - s)$, where $s = \omega/0.35$, is somewhat arbitrarily used to remove the singularities in the coefficient matrices. The linearization yields

$$\begin{bmatrix} -\widetilde{\mathbf{C}}_4^{-1}\widetilde{\mathbf{C}}_3 & -\widetilde{\mathbf{C}}_4^{-1}\widetilde{\mathbf{C}}_2 & -\widetilde{\mathbf{C}}_4^{-1}\widetilde{\mathbf{C}}_1 & -\widetilde{\mathbf{C}}_4^{-1}\widetilde{\mathbf{C}}_0 \\ \mathbf{I} & 0 & 0 & 0 \\ 0 & \mathbf{I} & 0 & 0 \\ 0 & 0 & \mathbf{I} & 0 \end{bmatrix} - \lambda\widetilde{\mathbf{I}} = 0 \tag{B13}$$

where $\mathbf{I}$ is the identity matrix of order $2N$ and $\widetilde{\mathbf{I}}$ is the identity matrix of order $8N$. The matrices $\widetilde{\mathbf{C}}_1$ to $\widetilde{\mathbf{C}}_4$ are nonsingular as a result of the applied eigenvalue shift. The eigenvalues and corresponding eigenvectors are found from equation (B13) by using the QR algorithm.

Local Method

The second solver is a more efficient local eigenvalue refiner referred to as the Lancaster refinement method (ref. 54). The method requires a sufficiently accurate initial estimate of the eigenvalue, which can be obtained from the above global method. The iterative formula is given by

$$\alpha^{i+1} = \alpha^i - 2f(\alpha^i)/[f^2(\alpha^i) - f^{(1)}(\alpha^i)] \tag{B14a}$$

where

$$f(\alpha^i) = \mathrm{Tr}[\mathbf{B}^{-1}(\alpha^i)\mathbf{B}^{(1)}(\alpha^i)] \tag{B14b}$$

$$f^{(1)}(\alpha^i) = \mathrm{Tr}\{\mathbf{B}^{-1}(\alpha^i)\mathbf{B}^{(2)}(\alpha^i) - [\mathbf{B}^{-1}(\alpha^i)\mathbf{B}^{(1)}(\alpha^i)]^2\} \tag{B14c}$$

and Tr is the matrix trace, $\mathbf{B}^{-1}$ is the inverse of $\mathbf{B}$ (from eqs. (B12)), and $\mathbf{B}^{(j)}$ denotes the jth derivative of $\mathbf{B}$ with respect to α. Upon convergence on the eigenvalue, the eigenvector may efficiently be found by the inverse iteration formula

$$\mathbf{B}(\alpha)\{v^{k+1}, \Omega^{k+1}\}^T = \sigma\{v^k, \Omega^k\}^T \tag{B15}$$

where σ is a normalizing factor. The procedure converges in two or three iterations for an initial guess of $\{v^0, \Omega^0\}^T = [1, 1, \ldots, 1]^T$. Equation (B13) or (B15), with the continuity equation and the definition of normal vorticity, leads to the eigenfunctions $\{\hat{u}, \hat{v}, \hat{w}\}$ required for the inflow condition (eqs. (7) and (8)).

Appendix C

PSE Theory

For the present paper, it is important to test and to verify the accuracy of the numerical techniques for the spatial DNS procedure and to make a detailed comparison with results of PSE theory. For this reason, brief highlights of some of the important theoretical and computational aspects of the PSE theory are given below.

As discussed in section 2, the evolution of disturbances is governed by the unsteady partial differential equations (4) to (6). Instead of solving these equations directly as in the DNS approach, the PSE theory seeks approximate solutions of the parabolized version of equations (4) to (6). The approximation needed to parabolize the governing equations, as first suggested by Herbert (ref. 15) and Bertolotti (ref. 16), includes the following two assumptions: (1) the dependence of the convected disturbance on downstream events is negligible and (2) no rapid streamwise variation (i.e., $\partial^2/\partial x^2 << 1$) occurs in the wavelength, the growth rate, the mean velocity profile, and all disturbance profiles.

For nonlinear disturbances present in the flow field, periodicity in both the time domain and the spanwise domain is assumed and the total disturbance in the following Fourier series expansion is

$$\mathbf{u}(x,y,z,t) = \sum_{m=-N_z}^{N_z} \sum_{n=-N_t}^{N_t} \hat{\mathbf{u}}_{m,n}(x,y) e^{mi\beta z - ni\omega t} \tag{C1}$$

where N_z and N_t are total numbers of modes kept in the truncated series and ω and β are the corresponding frequency and spanwise wave number. Equations (C1) are for velocity components; a similar expansion can be written for the pressure p. Through substitution of equations (C1) into the governing equations (4) to (6), a set of elliptic equations for the transformed variable $\hat{\mathbf{u}}_{m,n}$ $\hat{p}_{m,n}$ is obtained. Because of the wave nature of these transformed variables, they are decomposed into a fast-oscillatory wave part and a slow-varying shape function part as

$$\{\hat{\mathbf{u}}_{m,n}, \hat{p}_{m,n}\} = \{\tilde{\mathbf{u}}_{m,n}, \tilde{p}_{m,n}\} e^{i\alpha_{m,n}x} \tag{C2}$$

The governing equations now reduce to a set of partial differential equations for shape functions $\{\tilde{\mathbf{u}}_{m,n}, \tilde{p}_{m,n}\}$. In equation (C2), the fast-scale variation along the streamwise direction x is now represented by the streamwise wave number $\alpha_{m,n}$, and therefore the second-order variation of shape function in x is negligible (based on assumption 2 above). This observation leads to the parabolized stability equations for the shape functions, which are obtained by neglecting all second derivatives in the streamwise direction and the terms associated with upstream influence. In other words, through proper choice of $\alpha_{m,n}$, the evolution of disturbances can then be described by the parabolized equations for the shape functions.

Based on decomposition equations (C1) and (C2), the linear PSE can be derived for any disturbance with given frequency and spanwise wave number. For nonlinear problems, the following nonlinear terms must be added to the governing equations:

$$\mathbf{F}(x,y,z,t) = (\mathbf{u} \cdot \nabla)\mathbf{u} \tag{C3}$$

Since in the PSE approach the governing equations are solved in the wave number space, equation (C3) is expanded to a truncated Fourier series in the wave number space. The Fourier coefficients then provide a nonlinear forcing to each of the linearized shape function equations. These inhomogeneous equations for the shape functions are solved by a marching procedure along the streamwise direction for all Fourier modes.

Numerically, a second-order backward differencing is employed to integrate the equations in the streamwise direction. High-order finite-difference schemes (fourth-order) are employed to discretize the normal derivatives. The form of boundary conditions required for the PSE approach is of particular interest. Similar to the DNS approach, no-slip conditions are applied at the wall. The fundamental wave and harmonics vanish in the far field. To account for the change of displacement thickness in the perturbed boundary-layer flow, the far-field normal velocity gradients vanish for the mean-flow distortion equations.

Chang et al. (ref. 46) have extended the PSE numerical approach to the study of compressible boundary layers. With the PSE approach of Chang et al. for $M_\infty = 0$ and the incompressible results of Bertolotti (ref. 16), the present comparison with the DNS results is made.

Appendix D

Finite Difference Relations

The fourth-order finite-difference derivatives at the boundary $(0, N_x)$ and near-boundary $(1, N_x - 1)$ nodes are listed below. The first derivatives are

$$f'_0 = \frac{1}{12h_x}(-25f_0 + 48f_1 - 36f_2 + 16f_3 - 3f_4)$$

$$f'_1 = \frac{1}{12h_x}(-3f_0 - 10f_1 + 18f_2 - 6f_3 + f_4)$$

$$f'_N = \frac{1}{12h_x}(25f_N - 48f_{N-1} + 36f_{N-2} - 16f_{N-3} + 3f_{N-4})$$

$$f'_{N-1} = \frac{1}{12h_x}(3f_N + 10f_{N-1} - 18f_{N-2} + 6f_{N-3} - f_{N-4}) \quad \text{(D1)}$$

The second derivatives are

$$f''_0 = \frac{1}{12h_x^2}(35f_0 - 104f_1 + 114f_2 - 56f_3 + 11f_3)$$

$$f''_1 = \frac{1}{12h_x^2}(11f_0 - 20f_1 + 64f_2 + 4f_3 - f_4)$$

$$f''_N = \frac{1}{12h_x^2}(35f_N - 104f_{N-1} + 114f_{N-2} - 56f_{N-3} + 11f_{N-4})$$

$$f''_{N-1} = \frac{1}{12h_x^2}(11f_N - 20f_{N-1} + 64f_{N-2} + 4f_{N-3} - f_{N-4}) \quad \text{(D2)}$$

References

1. Orr, William M'F.: The Stability or Instability of the Steady Motions of a Perfect Liquid and of a Viscous Liquid. Part I.: A Perfect Liquid. *Proc. Royal Irish Acad.*, vol. XXVII, section A, no. 2, Mar. 1907, pp. 9–68.

2. Orr, William M'Fadden: The Stability or Instability of the Steady Motions of a Liquid. Part II.: A Viscous Liquid. *Proc. Royal Irish Acad.*, vol. XXVII, section A, no. 3, Oct. 1907, pp. 69–138.

3. Sommerfeld A.: Ein Beitrag zur Hydrodynamischen Erklaerung der Turbulenten Fluessigkeitsbewegungen. *Atti del 4.* Congressio Internazionale dei Matematica III (Rome), 1908, pp. 116–124.

4. Tollmien, W. (Dwight M. Miner, transl.): *The Production of Turbulence.* NACA TM 609, 1931.

5. Schlichting H.: Über die Entstehung der Turbulenz in Einem Rotierenden Zylinder. *Math.-Phys. Kl.*, no. 2, 1932, pp. 160–198.

6. Schubauer, G. B.; and Skramstad, H. K.: *Laminar-Boundary-Layer Oscillations and Transition on a Flat Plate.* NASA Rep. 909, 1948.

7. Schubauer, G. B.; and Skramstad, H. K.: Laminar Boundary-Layer Oscillations and Stability of Laminar Flow. *J. Aeronaut. Sci.*, vol. 14, no. 2, Feb. 1947, pp. 69–78.

8. Smith, A. M. O.; and Gamberoni, Nathalie: *Transition, Pressure Gradient, and Stability Theory.* Rep. No. ES 26388, Douglas Aircraft Co., Inc., Aug. 31, 1956. (Available in *IX Congrès International de Mécanique Appliquée,* Tome IV, Université die Bruxelles, 1957, pp. 234–244.)

9. Benney, D. J.; and Lin, C. C.: On the Secondary Motion Induced by Oscillations in a Shear Flow. *Phys. Fluids,* vol. 3, no. 4, July–Aug. 1960, pp. 656–657.

10. Craik, Alex D. D.: Non-Linear Resonant Instability in Boundary Layers. *J. Fluid Mech.*, vol. 50, pt. 2, Nov. 29, 1971, pp. 393–413.

11. Orszag, Steven A.; and Patera, Anthony T.: Subcritical Transition to Turbulence in Plane Channel Flows. *Phys. Review Lett.*, vol. 45, no. 12, Sept. 22, 1980, pp. 989–993.

12. Herbert, Thorwald: Secondary Instability of Shear Flows. *Special Course on Stability and Transition of Laminar Flow,* AGARD-R-709, June 1984, pp. 7-1–7-13.

13. Klebanoff, P. S.; Tidstrom, K. D.; and Sargent, L. M.: The Three-Dimensional Nature of Boundary-Layer Instability. *J. Fluid Mech.*, vol. 12, pt. 1, Jan. 1962, pp. 1–34.

14. Kachanov, Yu. S.; and Levchenko, V. Ya.: The Resonant Interaction of Disturbances at Laminar-Turbulent Transition in a Boundary Layer. *J. Fluid Mech.*, vol. 138, Jan. 1984, pp. 209–247.

15. Herbert Th.: Boundary-Layer Transition—Analysis and Prediction Revisited. AIAA-91-0737, Jan. 1991.

16. Bertolotti, Fabio Paolo: Linear and Nonlinear Stability of Boundary Layers With Streamwise Varying Properties. Ph.D. Thesis, Ohio State Univ., 1991.

17. Smith, F. T.: Nonlinear Stability of Boundary Layers for Disturbances of Various Sizes. *Proc. Royal Soc. London,* ser. A, vol. 368, no. 1735, Nov. 29, 1979, pp. 573–589.

18. Hall, P.; and Smith, F. T.: *Nonlinear Tollmien-Schlichting/Vortex Interaction in Boundary Layers.* NASA CR-181698, ICASE Rep. No. 88-46, 1988.

19. Zang, T. A.; and Hussaini, M. Y.: Numerical Simulation of Nonlinar Interactions in Channel and Boundary-Layer Transition. *Nonlinear Wave Interactions in Fluids,* R. W. Miksad, T. R. Akylas, and T. Herbert, eds., American Soc. of Mechanical Engineers, 1987, pp. 131–145.

20. Zang, Thomas A.; and Hussaini, M. Yousuff: Multiple Paths to Subharmonic Laminar Breakdown in a Boundary Layer. *Phys. Review Lett.*, vol. 64, no. 6, Feb. 5, 1990, pp. 641–644.

21. Laurien, E.; and Kleiser, L.: Numerical Simulation of Boundary-Layer Transition and Transition Control. *J. Fluid Mech.*, vol. 199, Feb. 1989, pp. 403–440.

22. Rai, Man Mohan; and Moin, Parviz: Direct Numerical Simulation of Transition and Turbulence in a Spatially Evolving Boundary Layer. *A Collection of Technical Papers—AIAA 10th Computational Fluid Dynamics Conference,* June 1991, pp. 890–914. (Available as AIAA-91-1607-CP.)

23. Fasel, Hermann: Untersuchungen zum Problem des Grenzschichtumschlages durch Numerische Integration der Navier-Stokes-Gleichungen. Ph.D. Diss., Univ. of Stuttgart, June 1974.

24. Fasel, H.: Investigation of the Stability of Boundary Layers by a Finite-Difference Model of the Navier-Stokes Equations. *J. Fluid Mech.*, vol. 78, pt. 2, Nov. 23, 1976, pp. 355–383.

25. Fasel, H.; and Konzelmann, U.: Non-Parallel Stability of a Flat-Plate Boundary Layer Using the Complete Navier-Stokes Equations. *J. Fluid Mech.*, vol. 221, Dec. 1990, pp. 311–347.

26. Fasel, H. F.; Rist, U.; and Konzelmann, U.: Numerical Investigation of the Three-Dimensional Development in Boundary-Layer Transition. *AIAA J.*, vol. 28, Jan. 1990, pp. 29–37.

27. Spalart, P. R.: Direct Numerical Study of Leading-Edge Contamination. *Fluid Dynamics of Three-Dimensional Turbulent Shear Flows and Transition,* AGARD-CP-438, Apr. 1989, pp. 5-1–5-13.

28. Danabasoglu, G.; Biringen, S.; and Streett, C. L.: Numerical Simulation of Spatially-Evolving Instability Control in Plane Channel Flow. AIAA-90-1530, June 1990.

29. Kleiser, Leonhard; and Zang, Thomas A.: Numerical Simulation of Transition in Wall-Bounded Shear Flows. *Annual Review of Fluid Mechanics,* Volume 23, John L. Lumley, Milton Van Dyke, and Helen L. Reed, eds., Annual Reviews Inc., 1991, pp. 495–537.

30. Kral, L. D.; and Fasel, H. F.: Numerical Investigation of the Control of the Secondary Instability Process in Boundary Layers. AIAA-89-0984, Mar. 1989.

31. Kreiss, H.; and Oliger, J.: *Methods for the Approximate Solution of Time Dependent Problems.* GARP Publ. Ser. No. 10, World Meteorological Organization, International Council of Scientific Unions, 1973.

32. Hirsh, Richard S.: Higher Order Accurate Difference Solutions of Fluid Mechanics Problems by a Compact Differencing Technique. *J. Comput. Phys.*, vol. 19, no. 1, Sept. 1975, pp. 90–109.

33. Adam, Yves: Highly Accurate Compact Implicit Methods and Boundary Conditions. *J. Comput. Phys.*, vol. 24, no. 1, May 1977, pp. 10–22.

34. Carpenter, Mark H.; Gottlieb, David; and Abarbanel, Saul: *The Stability of Numerical Boundary Treatments for Compact High-Order Finite-Difference Schemes.* NASA CR-187628, ICASE Rep. No. 91-71, 1991.

35. Gottlieb, David; and Orszag, Steven A.: *Numerical Analysis of Spectral Methods: Theory and Applications.* Soc. for Industrial and Applied Mathematics, c.1977.

36. Gottlieb, David; Hussaini, M. Yousuff; and Orszag, S. A.: *Theory and Applications of Spectral Methods.* NASA CR-185818, ICASE Rep. No. 83-66, 1983.

37. Canuto, Claudio; Hussaini, M. Yousuff; Quarteroni, Alfio; and Zang, Thomas A.: *Spectral Methods in Fluid Dynamics.* Springer-Verlag, c.1988.

38. Boyd, J. P.: *Chebyshev & Fourier Spectral Methods. Volume 49 of Lecture Notes in Engineering.* C. A. Brebbia and S. A. Orszag, eds., Springer-Verlag, c.1989.

39. Grosch, Chester E.; and Orszag, Steven A.: Numerical Solution of Problems in Unbounded Regions: Coordinate Transforms. *J. Comput. Phys.*, vol. 25, no. 3, Nov. 1977, pp. 273–295.

40. Williamson, J. H.: Low-Storage Runge-Kutta Schemes. *J. Comput. Phys.*, vol. 35, no. 1, Mar. 15, 1980, pp. 48–56.

41. Streett, C. L.; and Hussaini, M. Y.: *Finite Length Effects in Taylor-Couette Flow.* NASA CR-178175, ICASE Rep. No. 86-59, 1986.

42. Fortin, M.; Peyret, R.; and Temam, R.: Numerical Solution of the Navier-Stokes Equations for an Incompressible Fluid. *J. Mec.*, vol. 10, Sept. 1971, pp. 357–390.

43. Streett, C. L.; and Macaraeg, M. G.: Spectral Multi-Domain for Large-Scale Fluid Dynamic Simulations. *Int. J. Appl. Numer. Math.*, vol. 6, Dec. 1989, pp. 123–139.

44. Jordinson, R.: The Flat Plate Boundary Layer. Part 1. Numerical Integration of the Orr-Sommerfeld Equation. *J. Fluid Mech.*, vol. 43, pt. 4, Oct. 2, 1970, pp. 801–811.

45. Reshotko, E.: Environment and Receptivity. *Special Course on Stability and Transition of Laminar Flow*, AGARD-R-709, June 1984, pp. 4-1–4-11.

46. Chang, Chau-Lyan; Malik, Mujeeb R.; Erlebacher, Gordon; and Hussaini, M. Y.: Compressible Stability of Growing Boundary Layers Using Parabolized Stability Equations. AIAA-91-1636, June 1991.

47. Prandtl, L.: *Motion of Fluids With Very Little Viscosity.* NACA TM 452, 1927.

48. Blasius, H. (J. Vanier, transl.): The Boundary Layers in Fluids With Little Friction. NACA TM 1256, 1950.

49. Luther, H. A.: Further Explicit Fifth-Order Runge-Kutta Formulas. *SIAM Review*, vol. 8, no. 3, July 1966, pp. 374–380.

50. Squire, H. B.: On the Stability for Three-Dimensional Disturbances of Viscous Fluid Flow Between Parallel Walls. *Proc. Royal Soc. London*, ser. A, vol. CXLII, Nov. 1933, pp. 621–628.

51. Joslin, Ronald Douglas: The Effect of Compliant Walls on Three-Dimensional Primary and Secondary Instabilities in Boundary Layer Transition. Ph.D. Thesis, Pennsylvania State Univ., 1990.

52. Gohberg, I.; Lancaster, P.; and Rodman, L.: *Matrix Polynomials.* Academic Press, 1982.

53. Bridges, Thomas J.; and Morris, Philip J.: Boundary Layer Stability Calculations. *Phys. Fluids*, vol. 30, no. 11, Nov. 1987, pp. 3351–3358.

54. Lancaster, P.: Algorithms for Lambda-Matrices. *Numer. Math.*, Band 6, 1964, pp. 388–394.

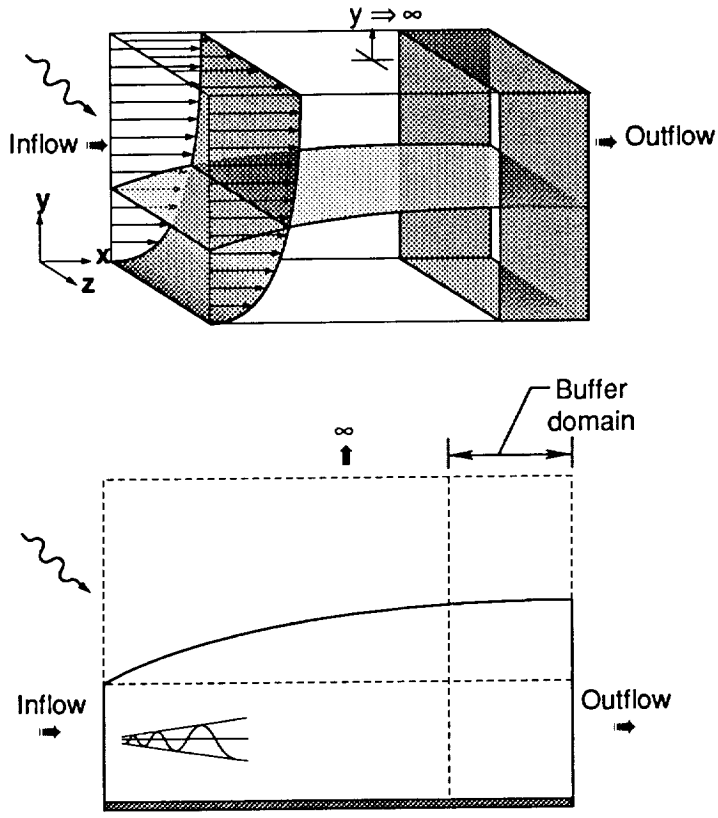

Figure 1. Computational domain for transitional boundary-layer problem.

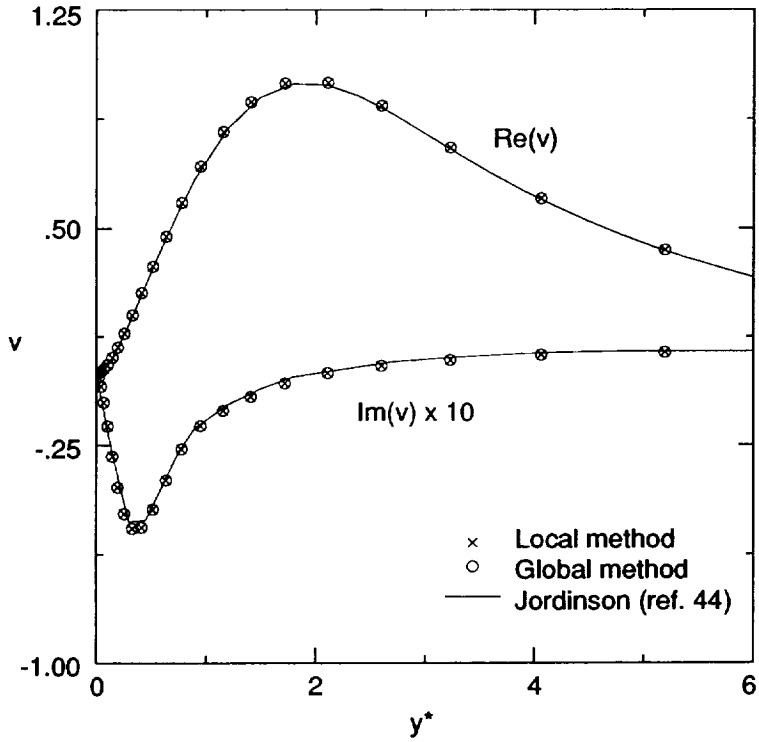

Figure 2. Eigenfunctions obtained with local and global spectral-collocation methods and from Jordinson (ref. 44). $N = 32; R^* = 998; \omega = 0.1122; \alpha = 0.3086 - i0.0057$.

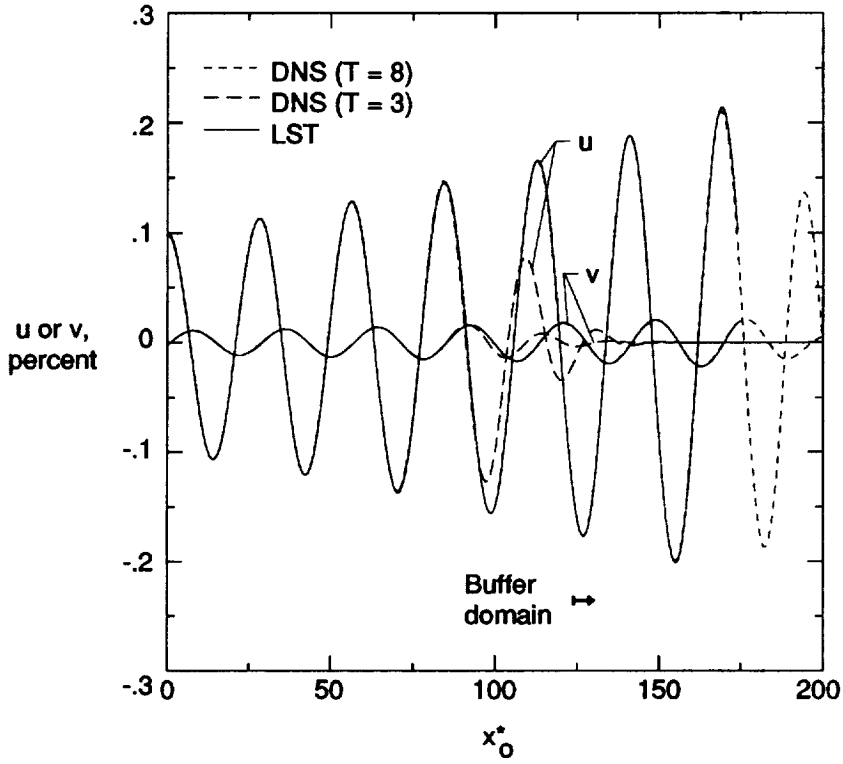

Figure 3. Amplitudes of streamwise and wall-normal velocity components of 2-D disturbance with downstream distance for parallel boundary layer for inflow. $R_o^* = 900$; $F_r = 86$; $A_{1,0}^o = 0.1$ percent.

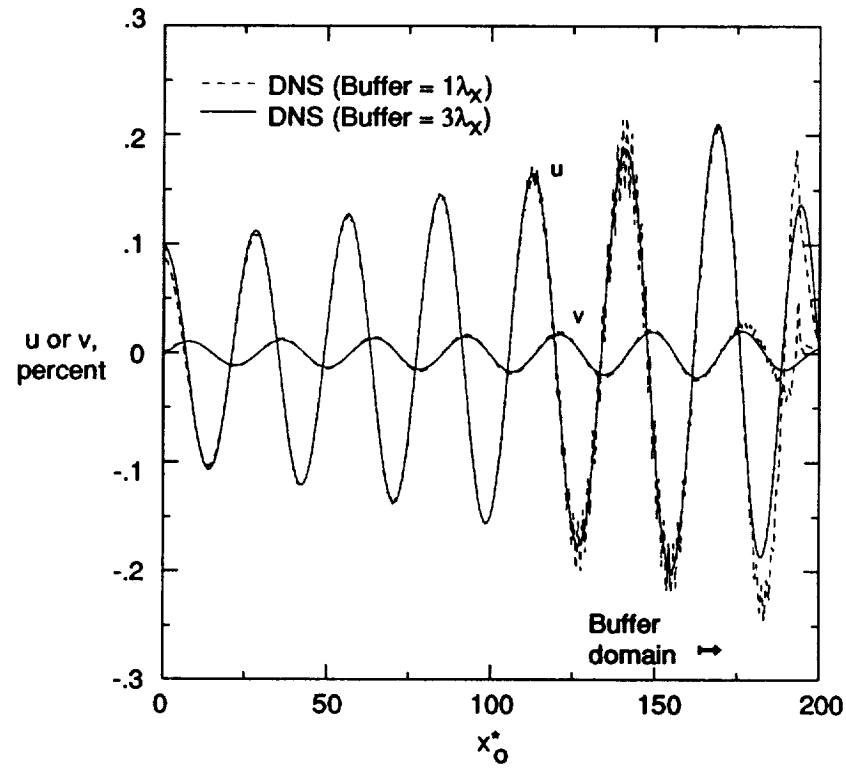

Figure 4. Amplitudes of streamwise and wall-normal velocity components of 2-D disturbance with downstream distance for parallel boundary layer for inflow with adequate and inadequate buffer regions. $R_o^* = 900$; $F_r = 86$; $A_{1,0}^o = 0.1$ percent.

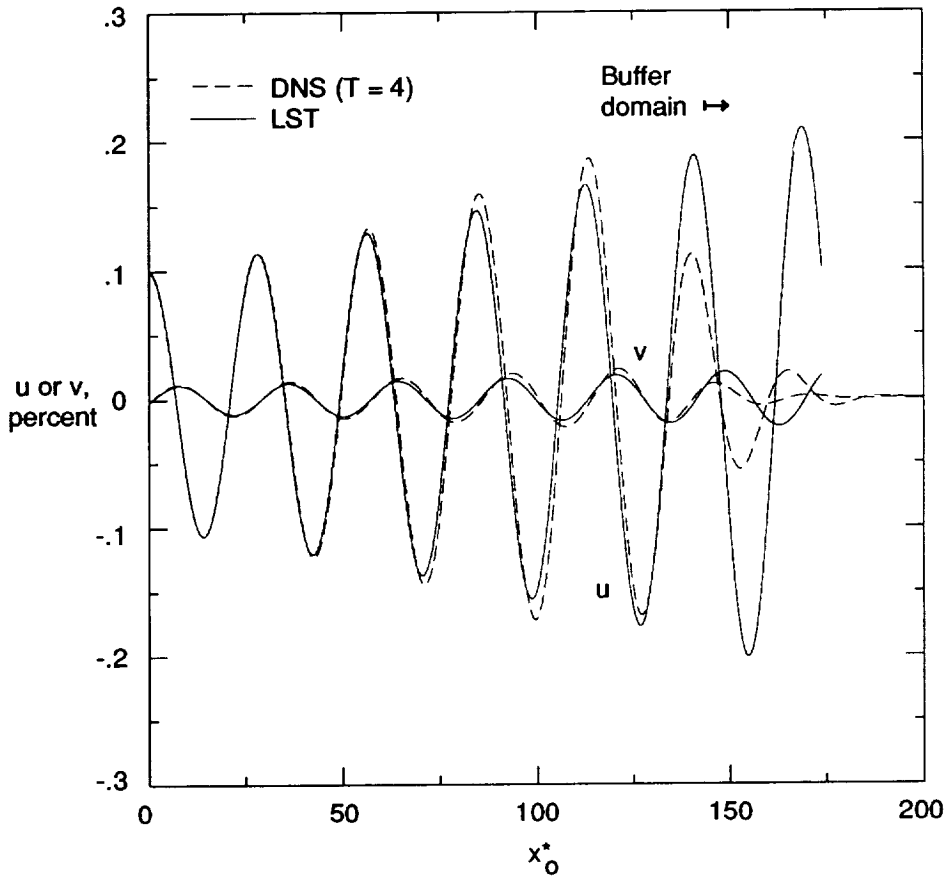

Figure 5. Amplitudes of streamwise and wall-normal velocity components of 2-D disturbance with downstream distance for nonparallel boundary layer for inflow. $R_o^* = 900$; $F_r = 86$; $A_{1,0}^o = 0.1$ percent.

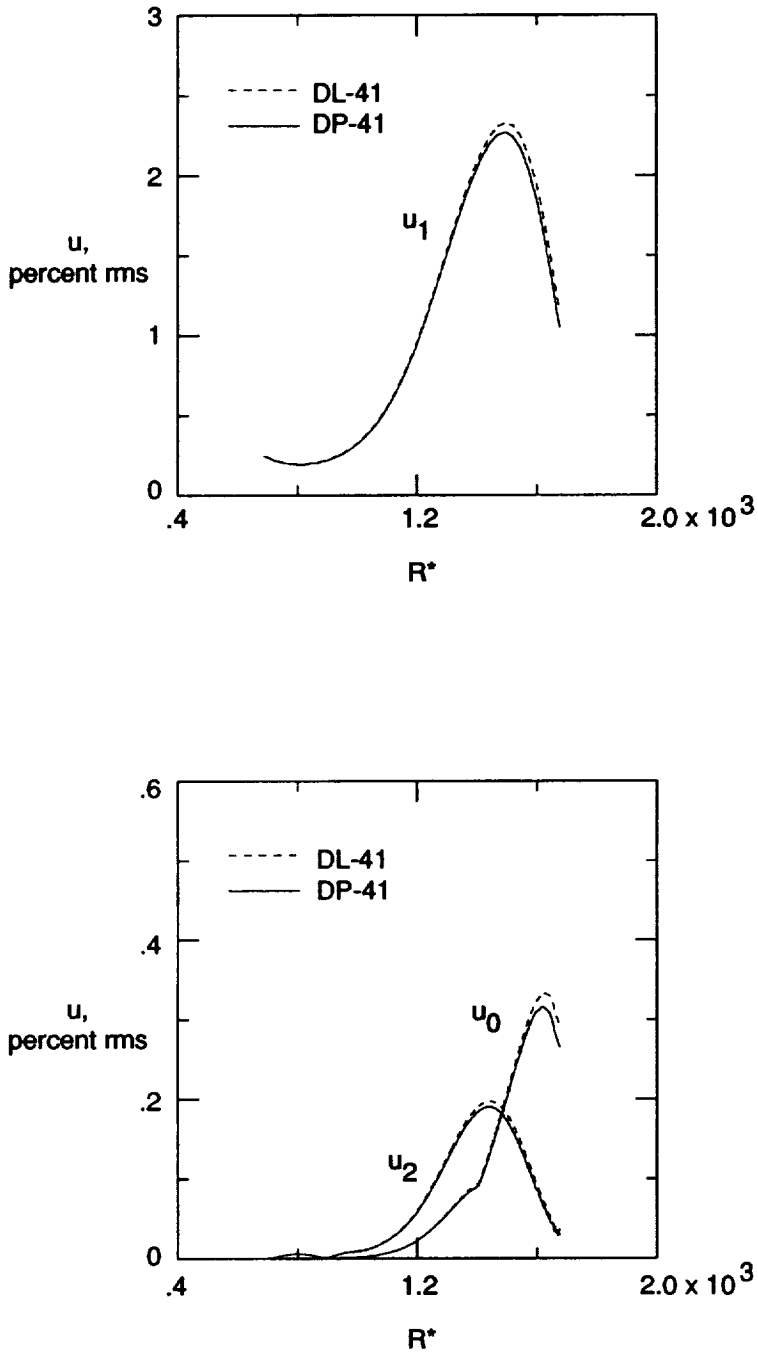

Figure 6. Maximum streamwise amplitudes of fundamental wave u_1, mean-flow distortion u_0, and first harmonic u_2 with Reynolds number (or downstream distance) for cases DP-41 and DL-41 with inflow. $R_o^* = 688.315$; $F_r = 86$; $A_{1,0}^o = 0.25$ percent.

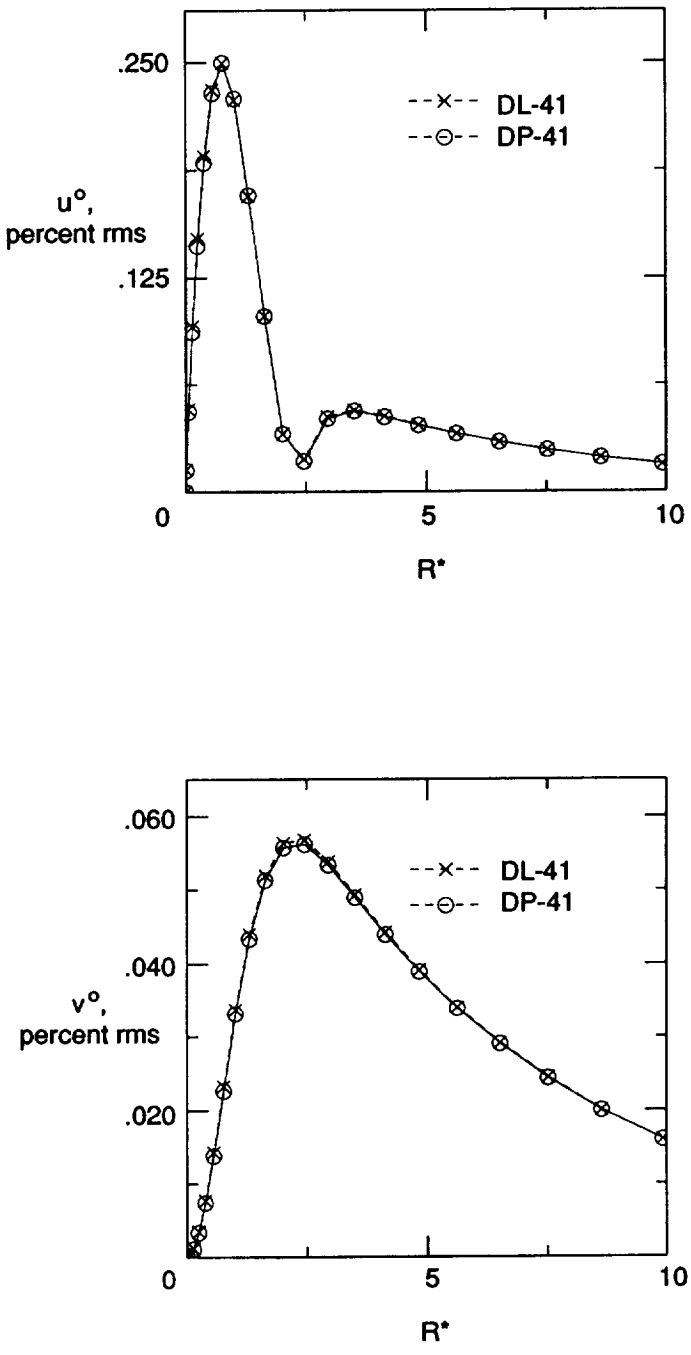

Figure 7. Streamwise and wall-normal velocity components of 2-D disturbance as predicted by LST and PSE for inflow. $R_o^* = 688.315$; $F_r = 86$; $A_{1,0}^0 = 0.25$ percent.

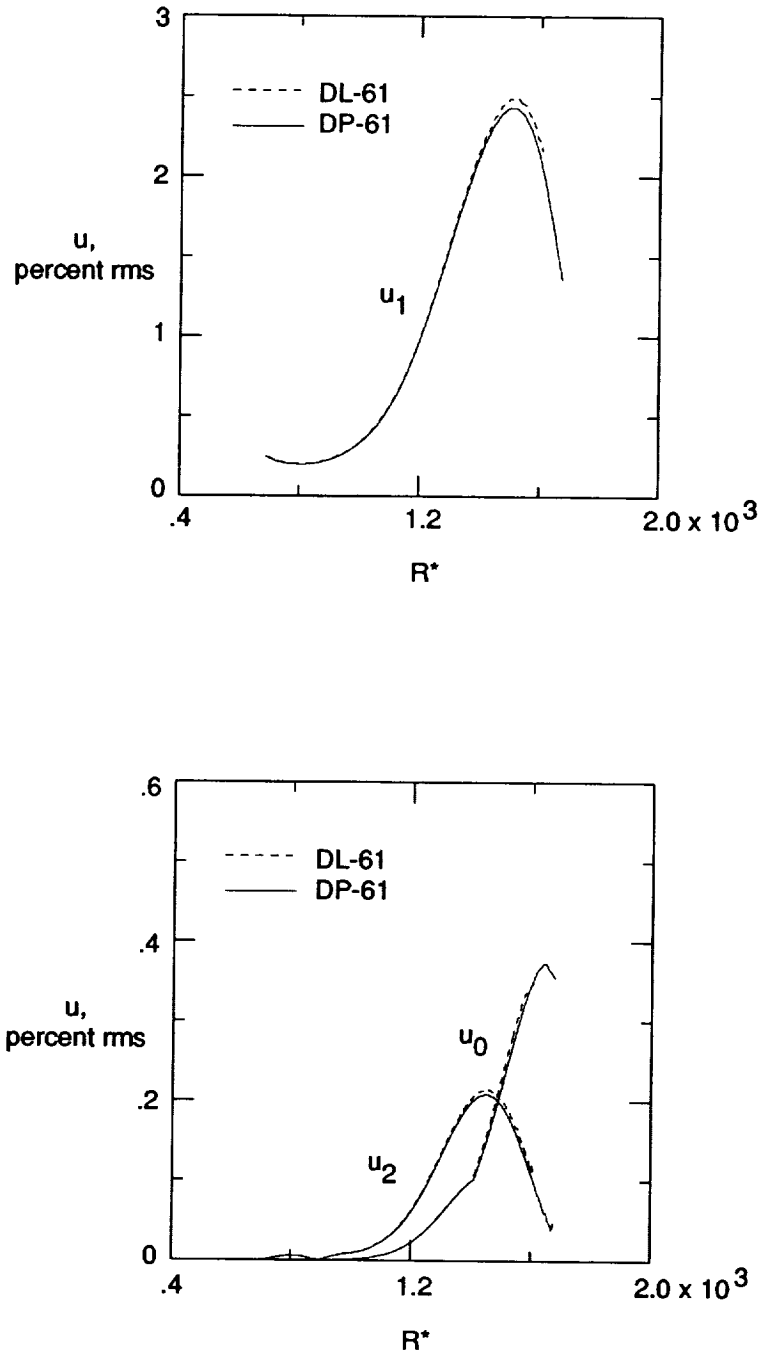

Figure 8. Maximum streamwise amplitudes of fundamental wave u_1, mean-flow distortion u_0, and first harmonic u_2 with Reynolds number (or downstream distance) for cases DP-61 and DL-61 with inflow. $R_o^* = 688.315$; $F_r = 86$; $A_{1,0}^o = 0.25$ percent.

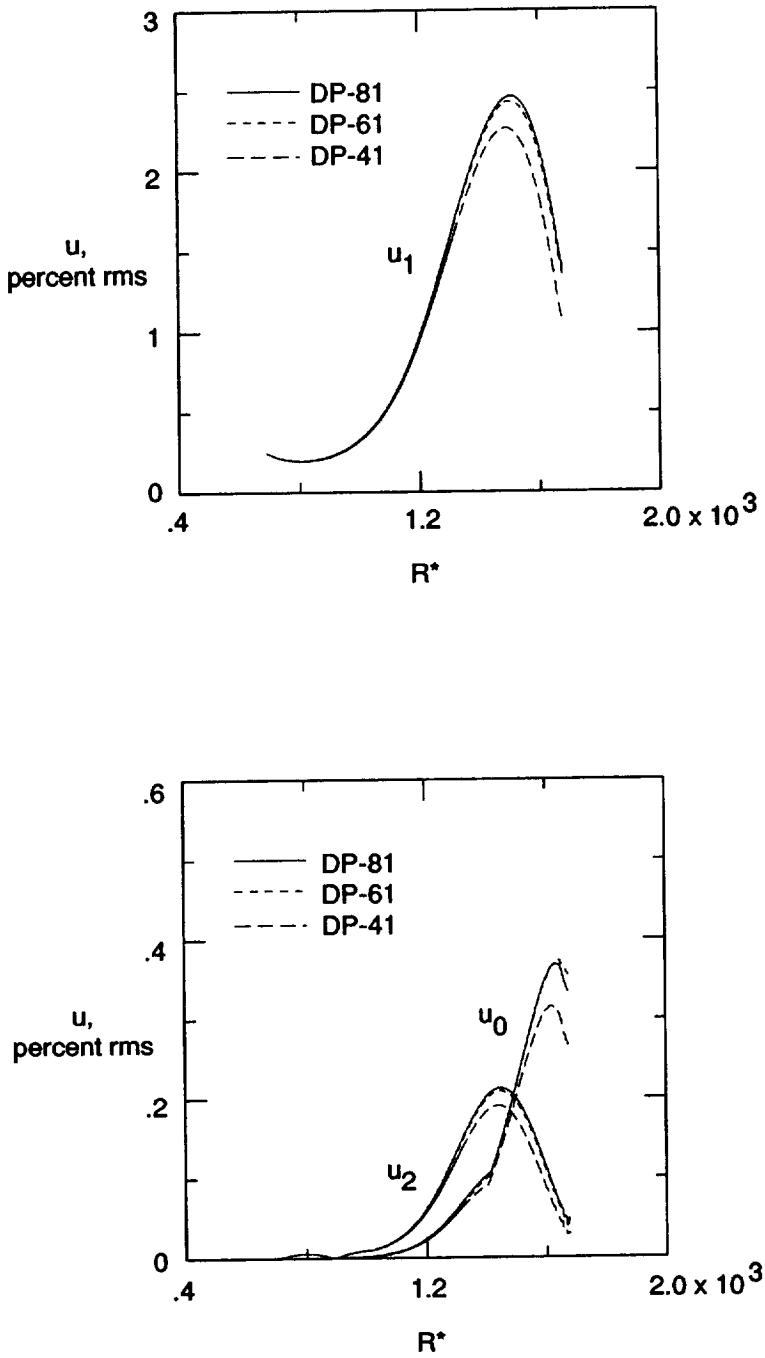

Figure 9. Maximum streamwise amplitudes of fundamental wave u_1, mean-flow distortion u_0, and first harmonic u_2 with Reynolds number (or downstream distance) for cases DP-81, DP-61, and DP-41 with inflow. $R_o^* = 688.315; F_r = 86; A_{1,0}^o = 0.25$ percent.

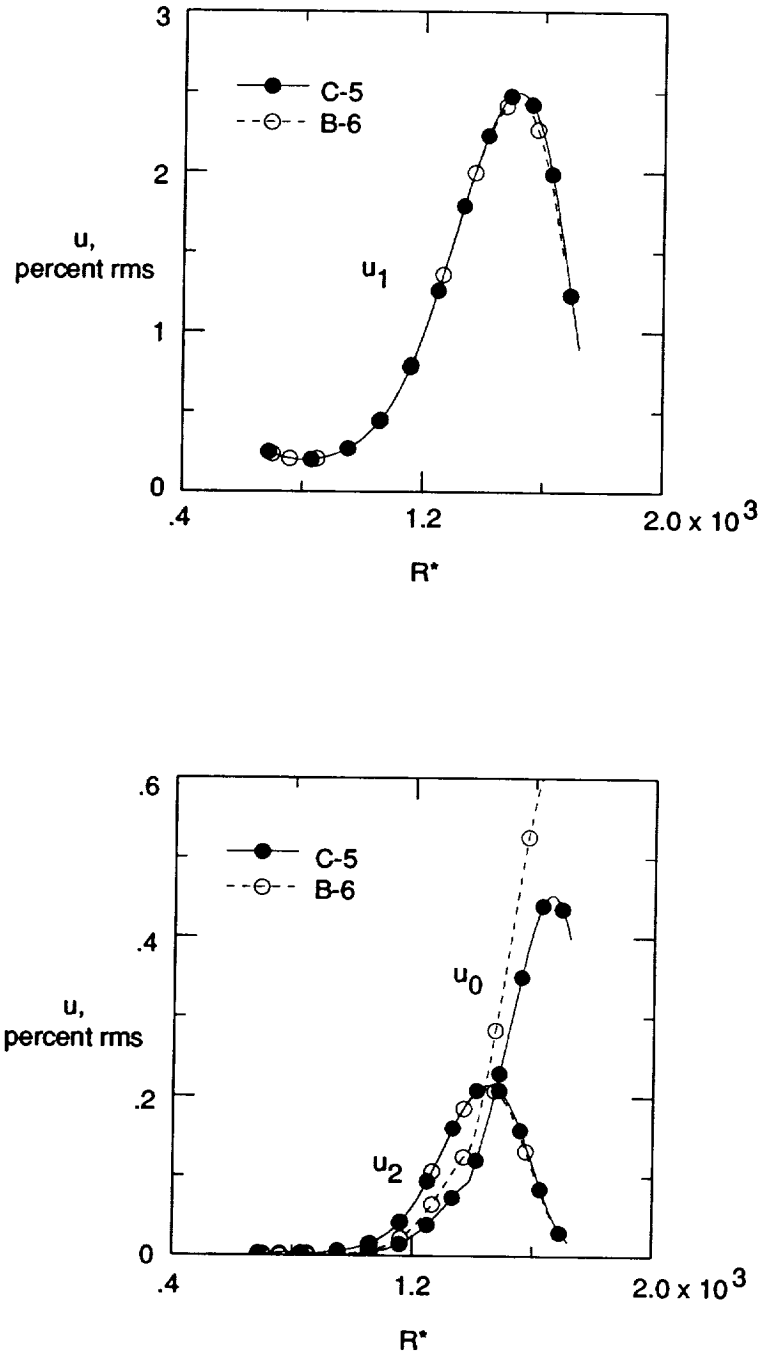

Figure 10. Maximum streamwise amplitudes of fundamental wave u_1, mean-flow distortion u_0, and first harmonic u_2 with Reynolds number (or downstream distance) for PSE cases C-5 and B-6 with inflow. $R_o^* = 688.315$; $F_r = 86$; $A_{1,0}^o = 0.25$ percent.

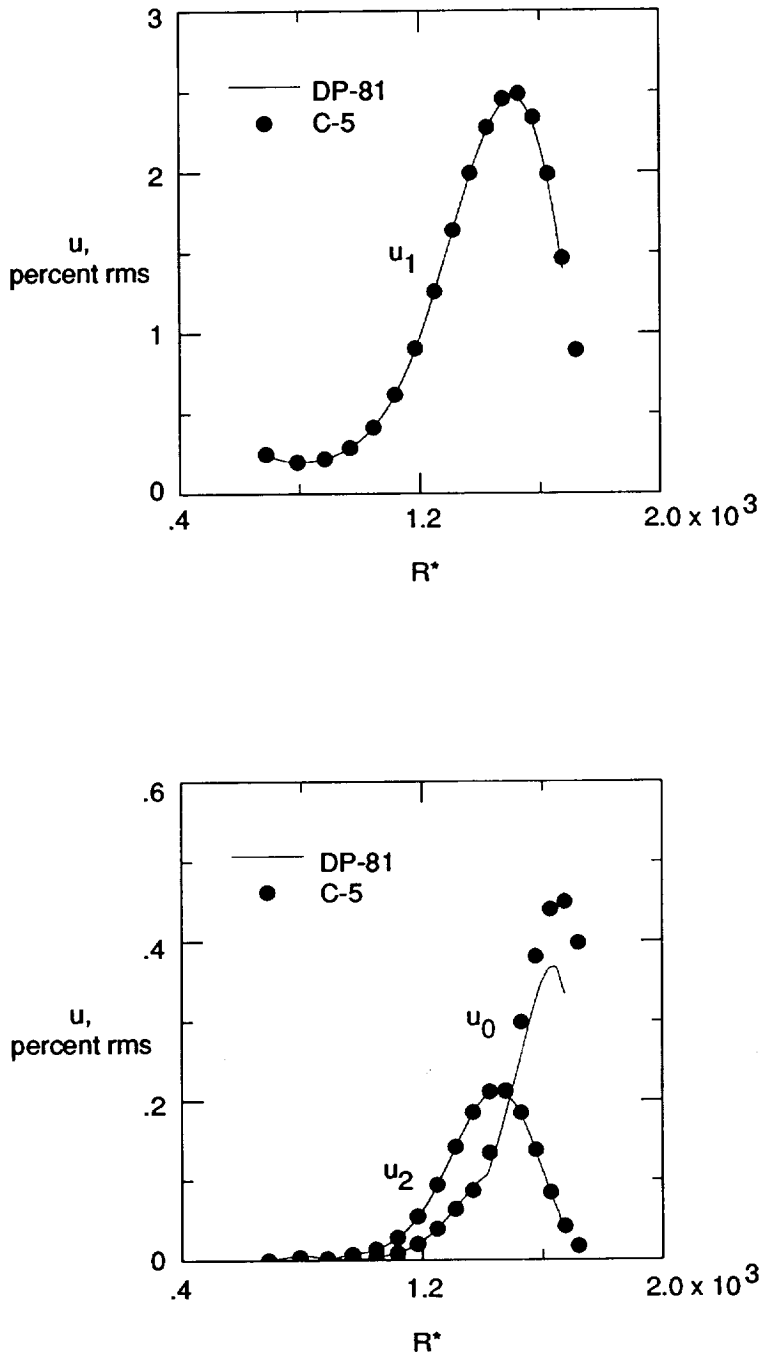

Figure 11. Maximum streamwise amplitudes of fundamental wave u_1, mean-flow distortion u_0, and first harmonic u_2 with Reynolds number (or downstream distance) for cases DP-81 and C-5 with inflow. $R_o^* = 688.315$; $F_r = 86$; $A_{1,0}^o = 0.25$ percent.

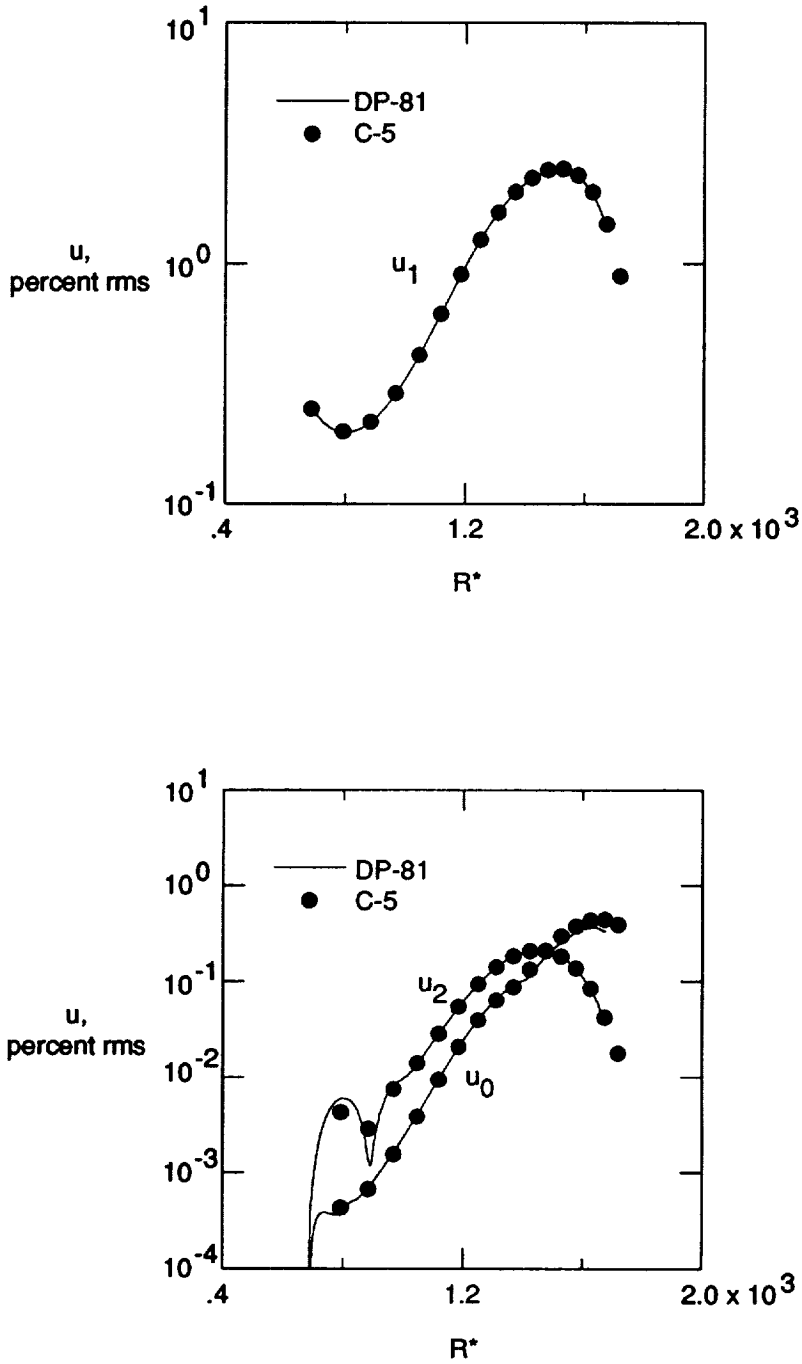

Figure 12. Logarithmic maximum streamwise amplitudes of fundamental wave u_1, mean-flow distortion u_0, and first harmonic u_2 with Reynolds number (or downstream distance) for cases DP-81 and C-5 with inflow. $R_o^* = 688.315$; $F_r = 86$; $A_{1,0}^o = 0.25$ percent.

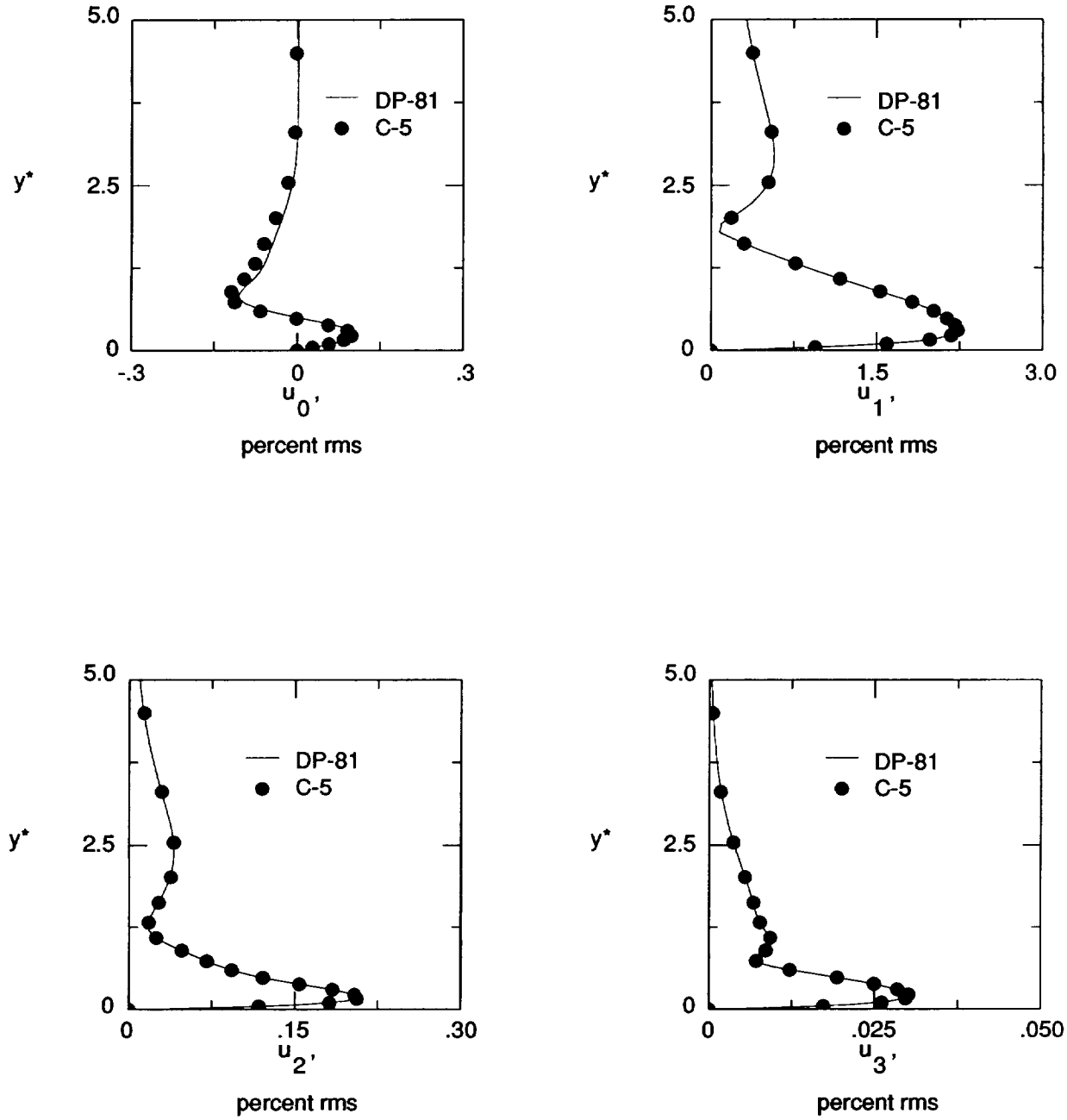

Figure 13. Streamwise disturbance profiles of mean-flow distortion u_0, fundamental wave u_1, and first and second harmonics u_2 and u_3 with normal distance from wall as predicted by cases DP-81 and C-5 for $R^* = 1413$.

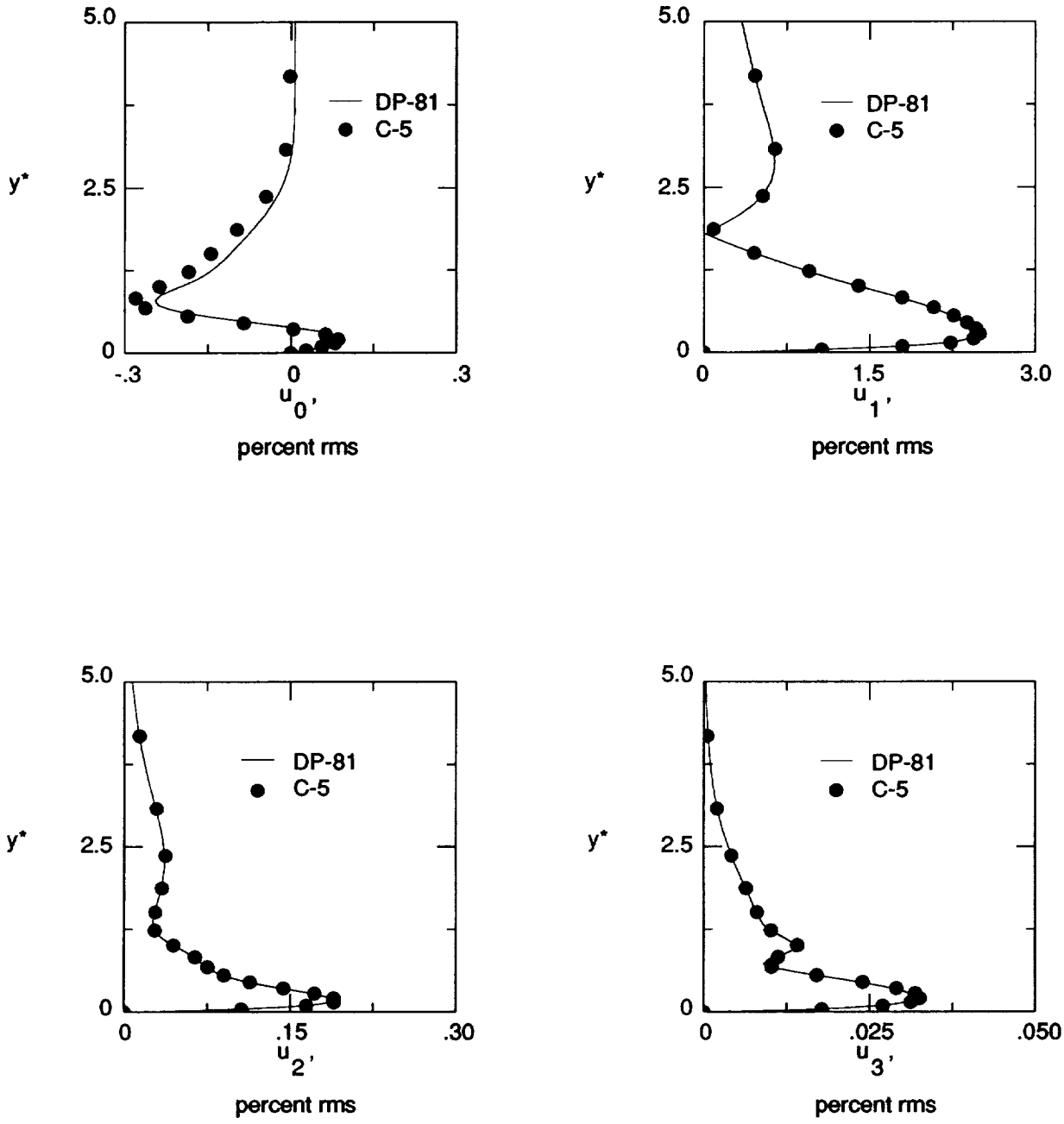

Figure 14. Streamwise disturbance profiles of mean-flow distortion u_0, fundamental wave u_1, and first and second harmonics u_2 and u_3 with normal distance from wall as predicted by cases DP-81 and C-5 for $R^* = 1519$.

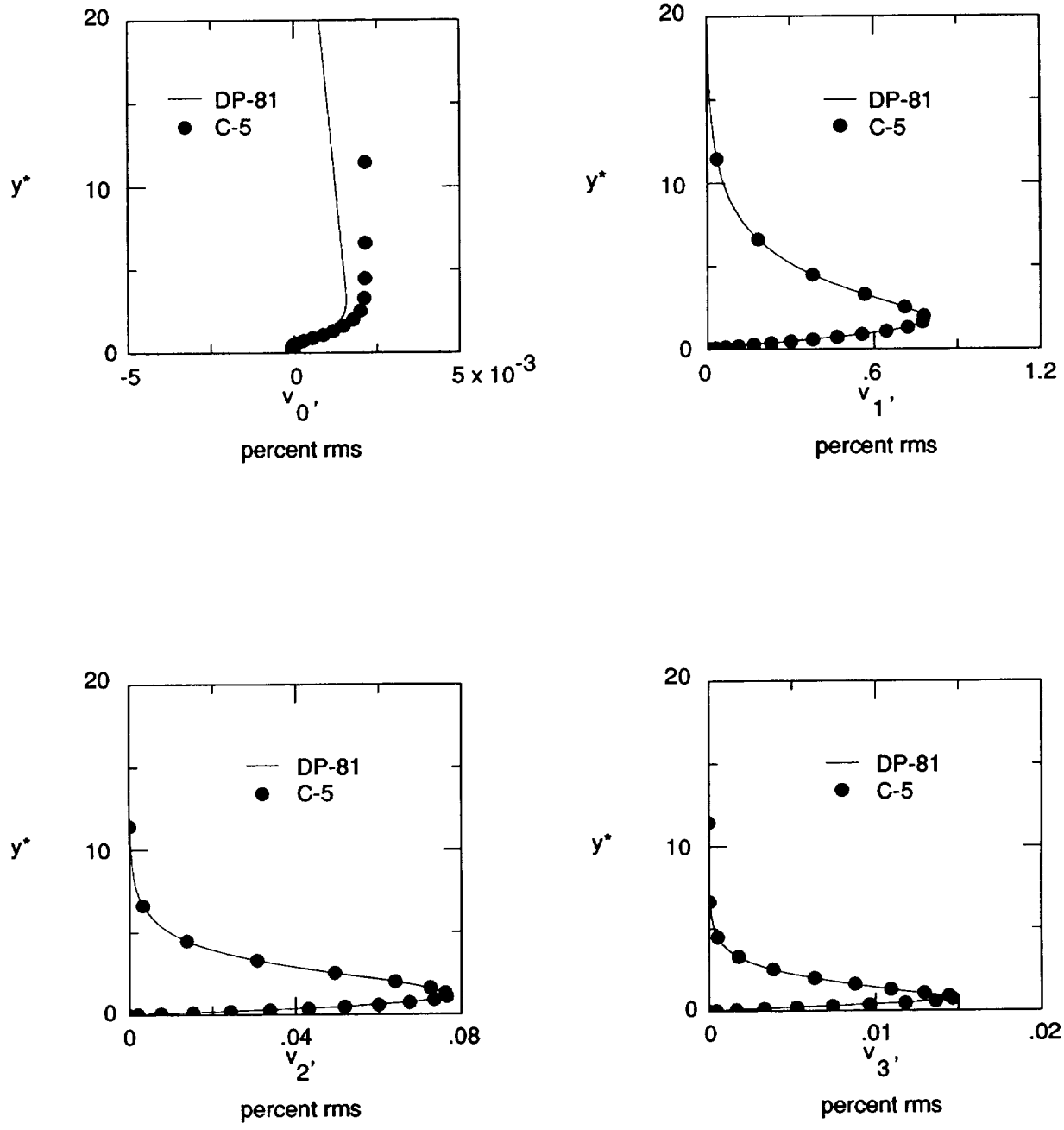

Figure 15. Wall-normal disturbance profiles of mean-flow distortion v_0, fundamental wave v_1, and first and second harmonics v_2 and v_3 with normal distance from wall as predicted by cases DP-81 and C-5 for $R^* = 1413$.

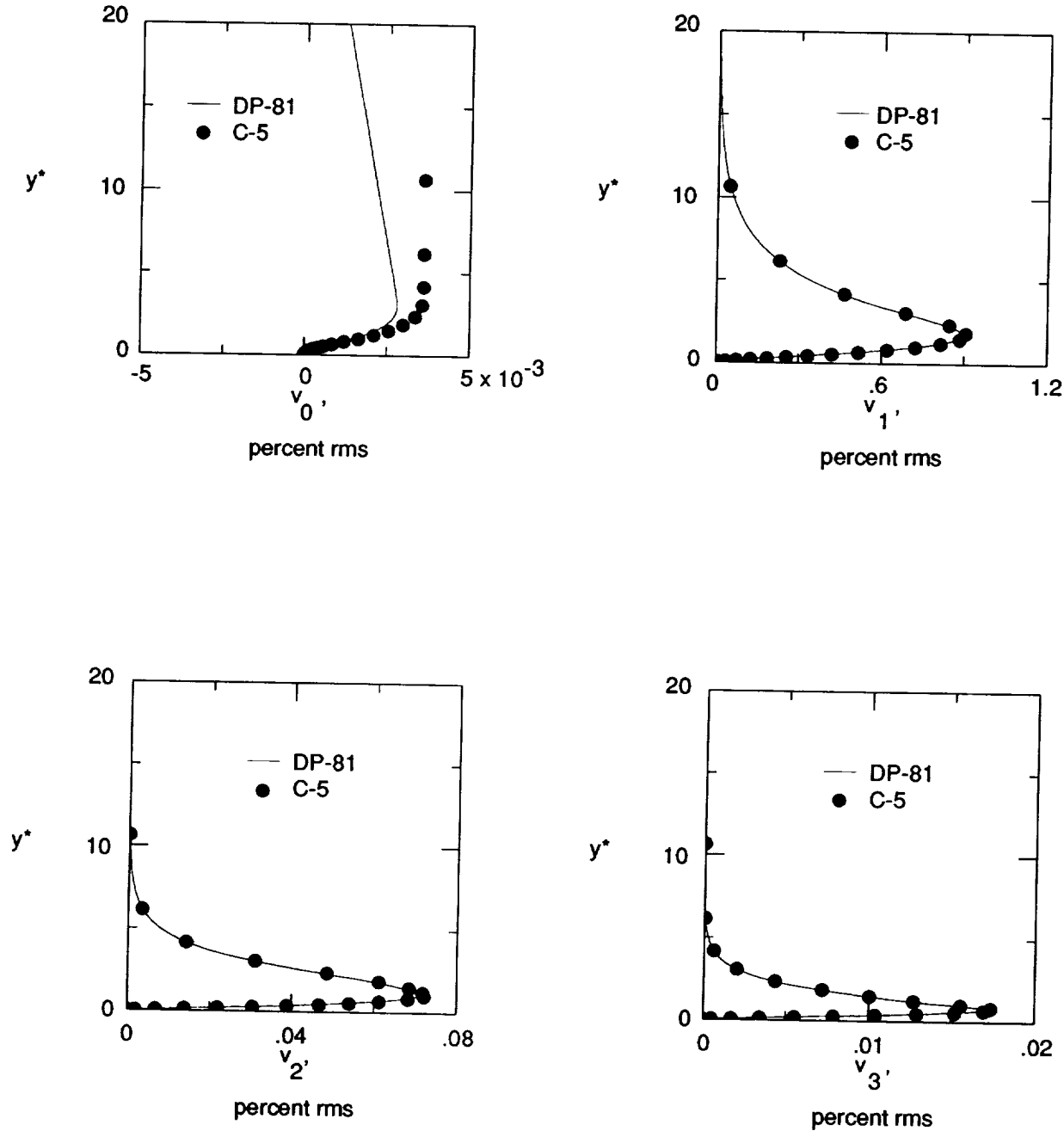

Figure 16. Wall-normal disturbance profiles of mean-flow distortion v_0, fundamental wave v_1, and first and second harmonics v_2 and v_3 with normal distance from wall as predicted by cases DP-81 and C-5 for $R^* = 1519$.

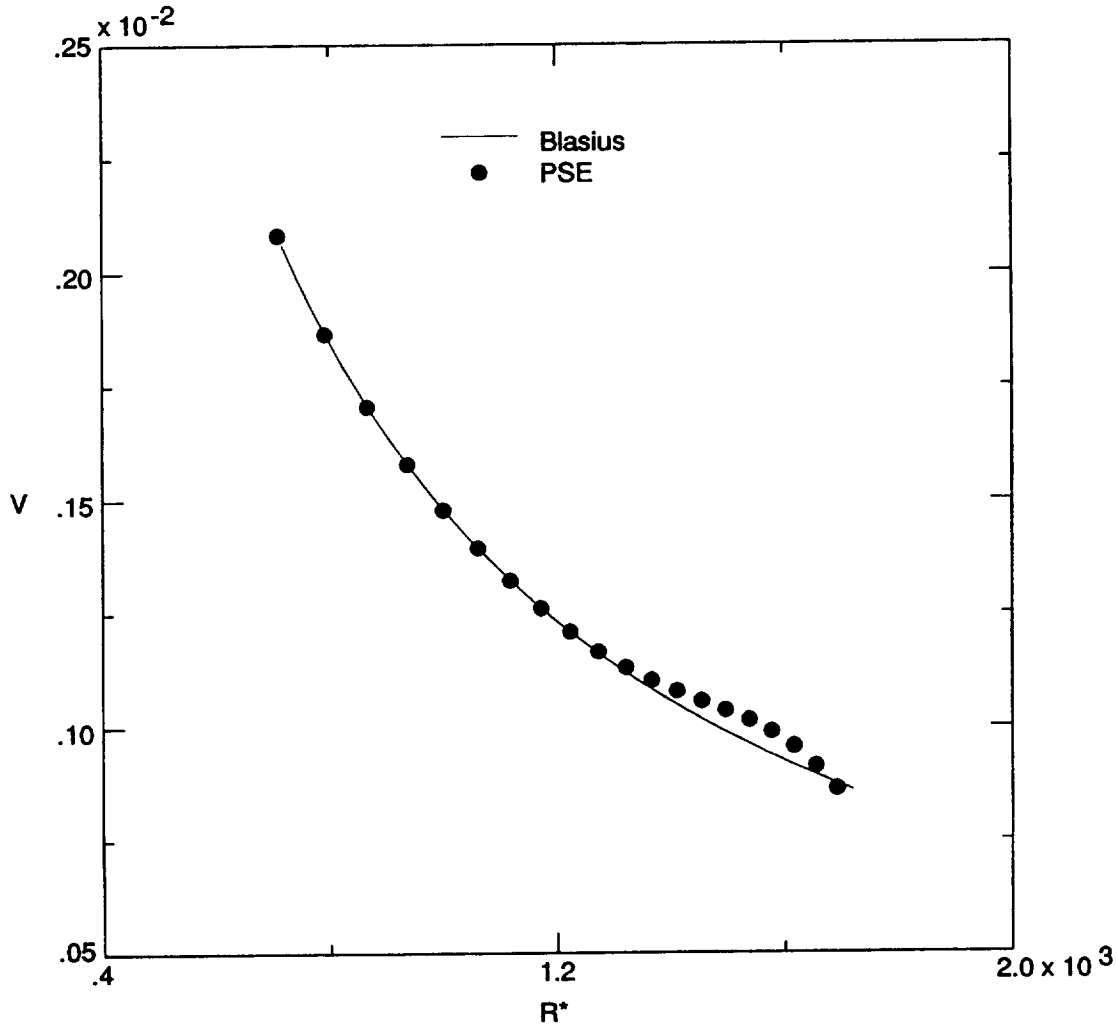

Figure 17. Wall-normal component of mean flow at far-field boundary for Blasius flow and from PSE theory.

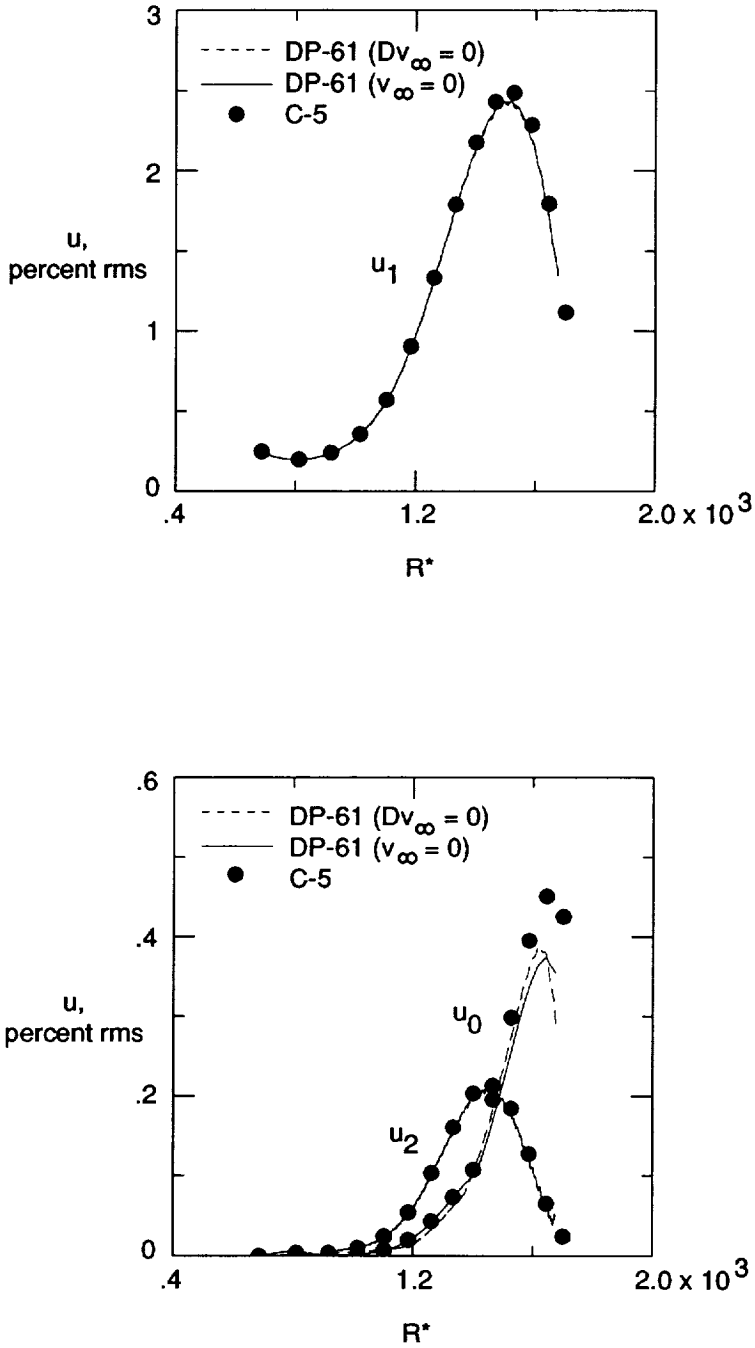

Figure 18. Maximum streamwise amplitude of fundamental wave u_1, mean-flow distortion u_0, and first harmonic u_2 with Reynolds number (or downstream distance) for cases DP-61 and C-5 with inflow. $R_o^* = 688.315$; $F_r = 86$; $A_{1,0}^o = 0.25$ percent.

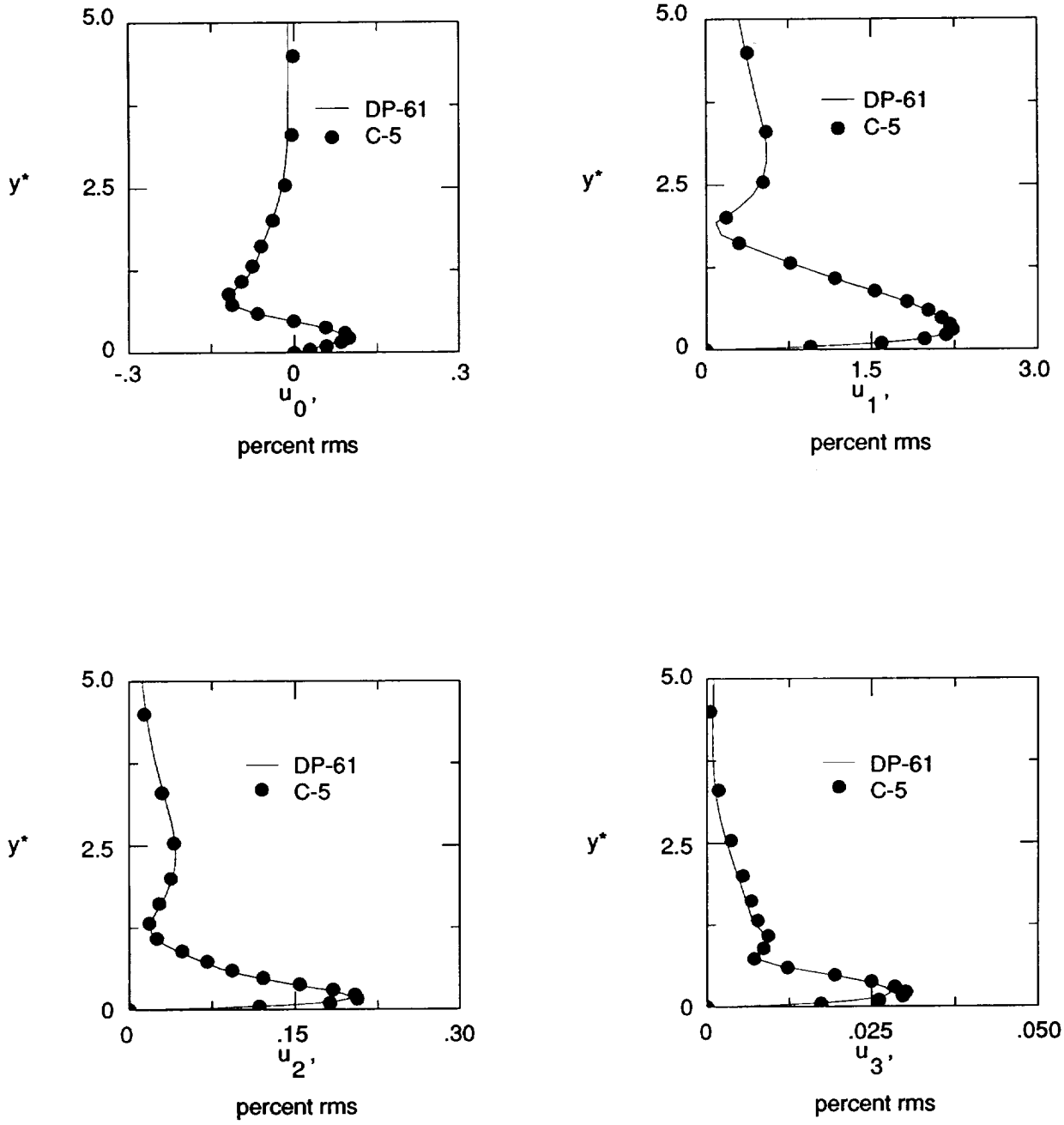

Figure 19. Streamwise disturbance profiles of mean-flow distortion u_0, fundamental wave u_1, and first and second harmonics u_2 and u_3 with normal distance from wall as predicted by cases DP-61 ($Dv_\infty = 0$) and C-5 for $R^* = 1413$.

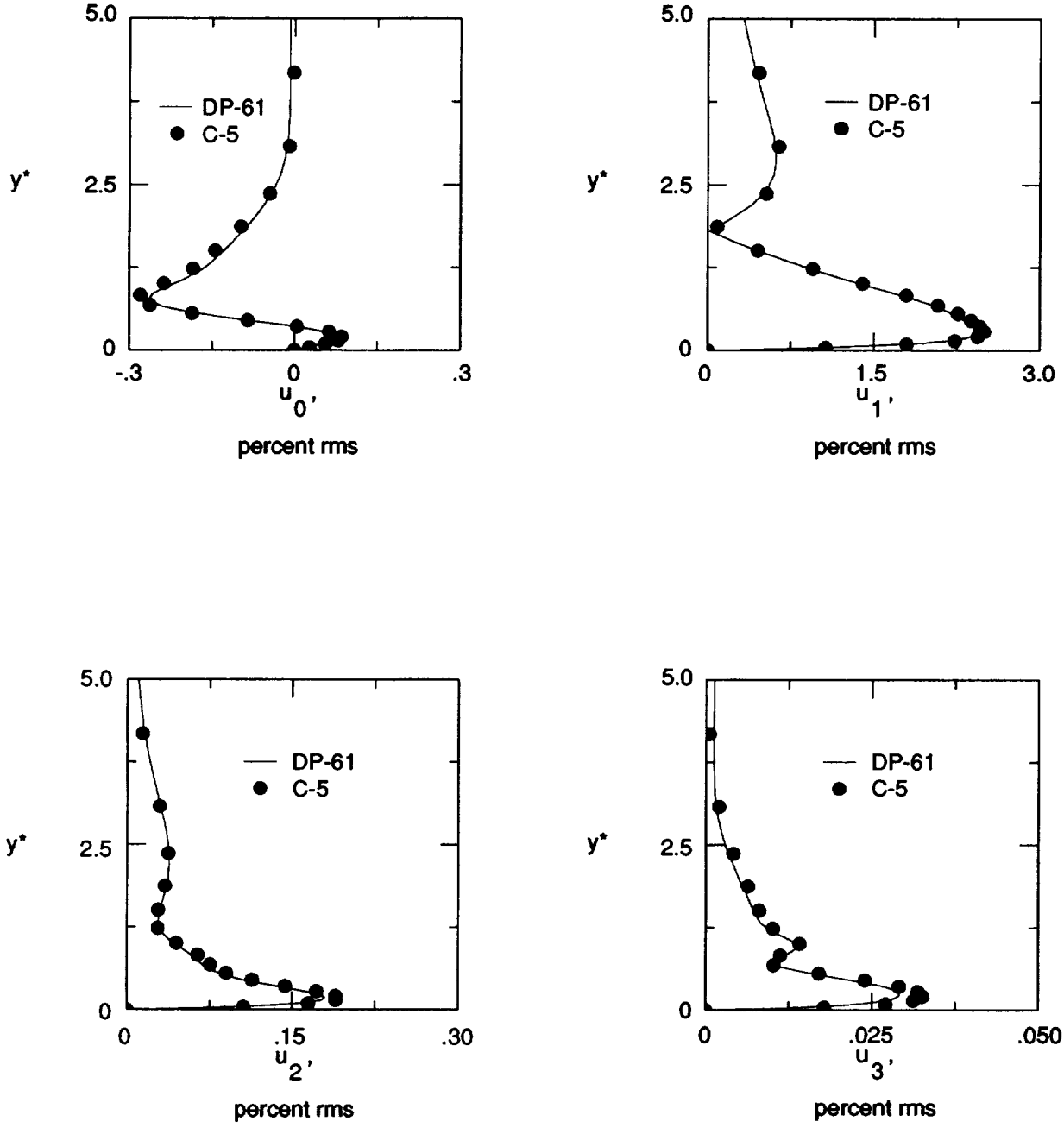

Figure 20. Streamwise disturbance profiles of mean-flow distortion u_0, fundamental wave u_1, and first and second harmonics u_2 and u_3 with normal distance from wall as predicted by cases DP-61 ($Dv_\infty = 0$) and C-5 for $R^* = 1519$.

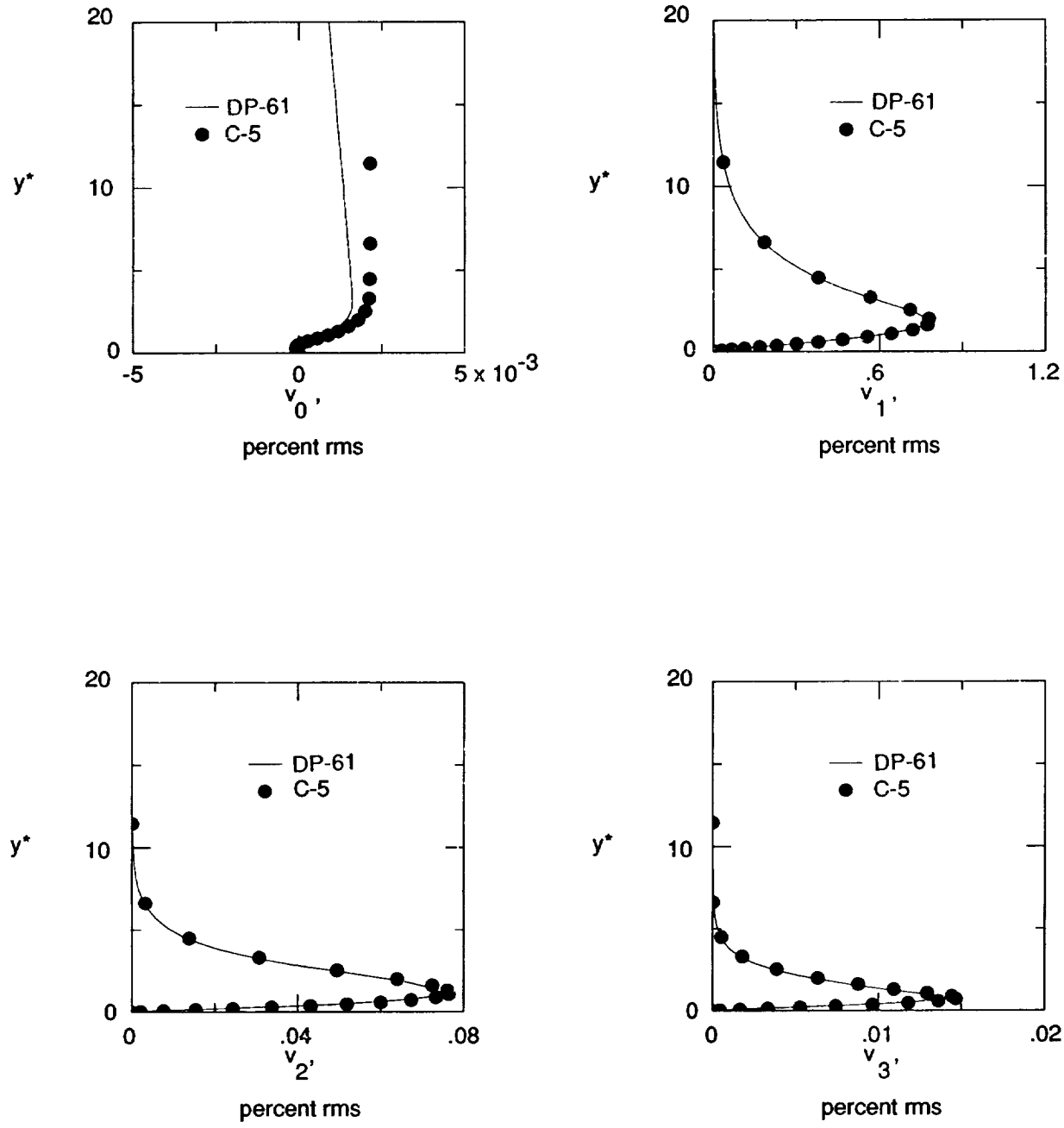

Figure 21. Wall-normal disturbance profiles of mean-flow distortion v_0, fundamental wave v_1, and first and second harmonics v_2 and v_3 with normal distance from wall as predicted by cases DP-61 ($Dv_\infty = 0$) and C-5 for $R^* = 1413$.

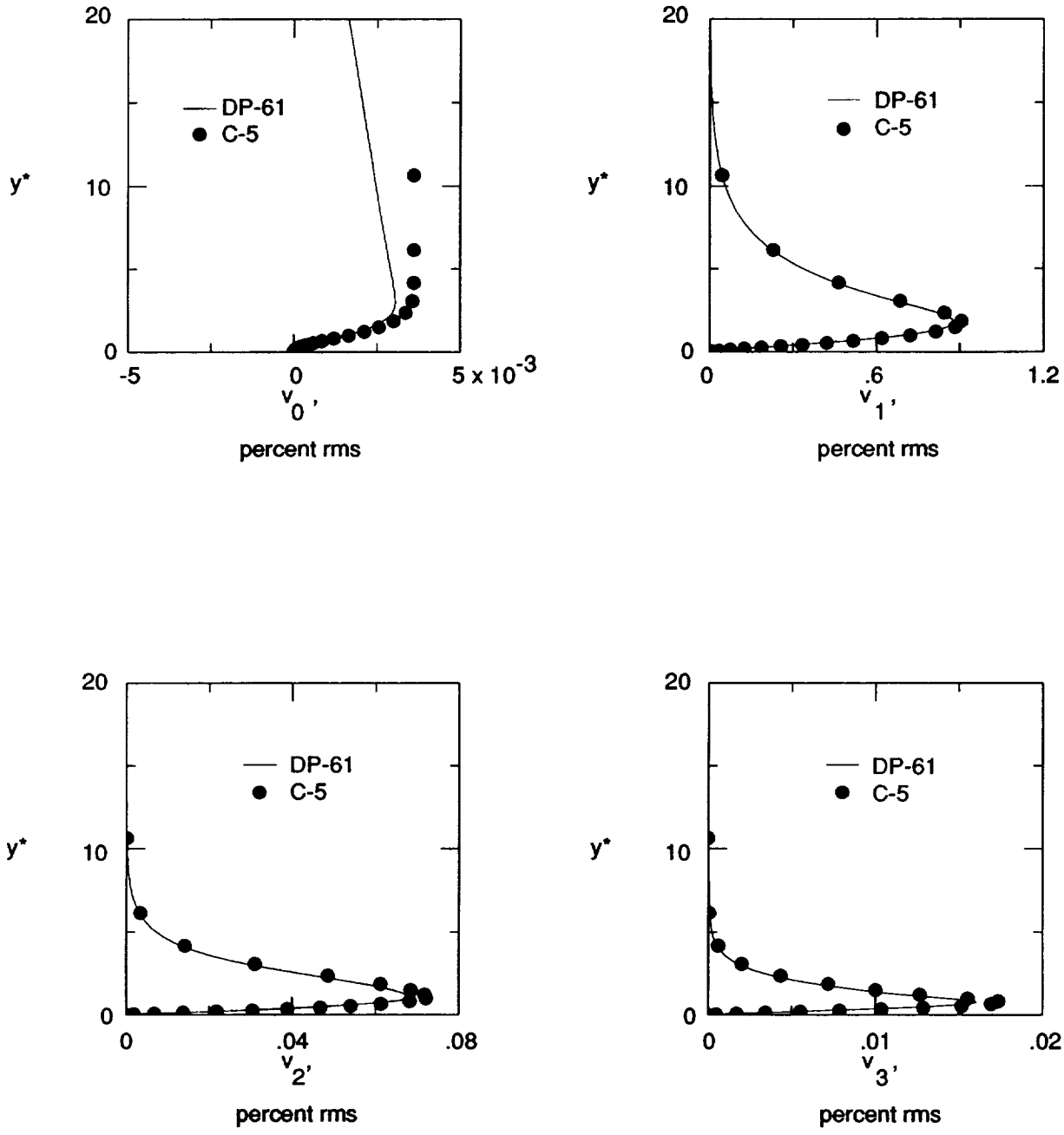

Figure 22. Wall-normal disturbance profiles of mean-flow distortion v_0, fundamental wave v_1, and first and second harmonics v_2 and v_3 with normal distance from wall as predicted by cases DP-61 ($Dv_\infty = 0$) and C-5 for $R^* = 1519$.

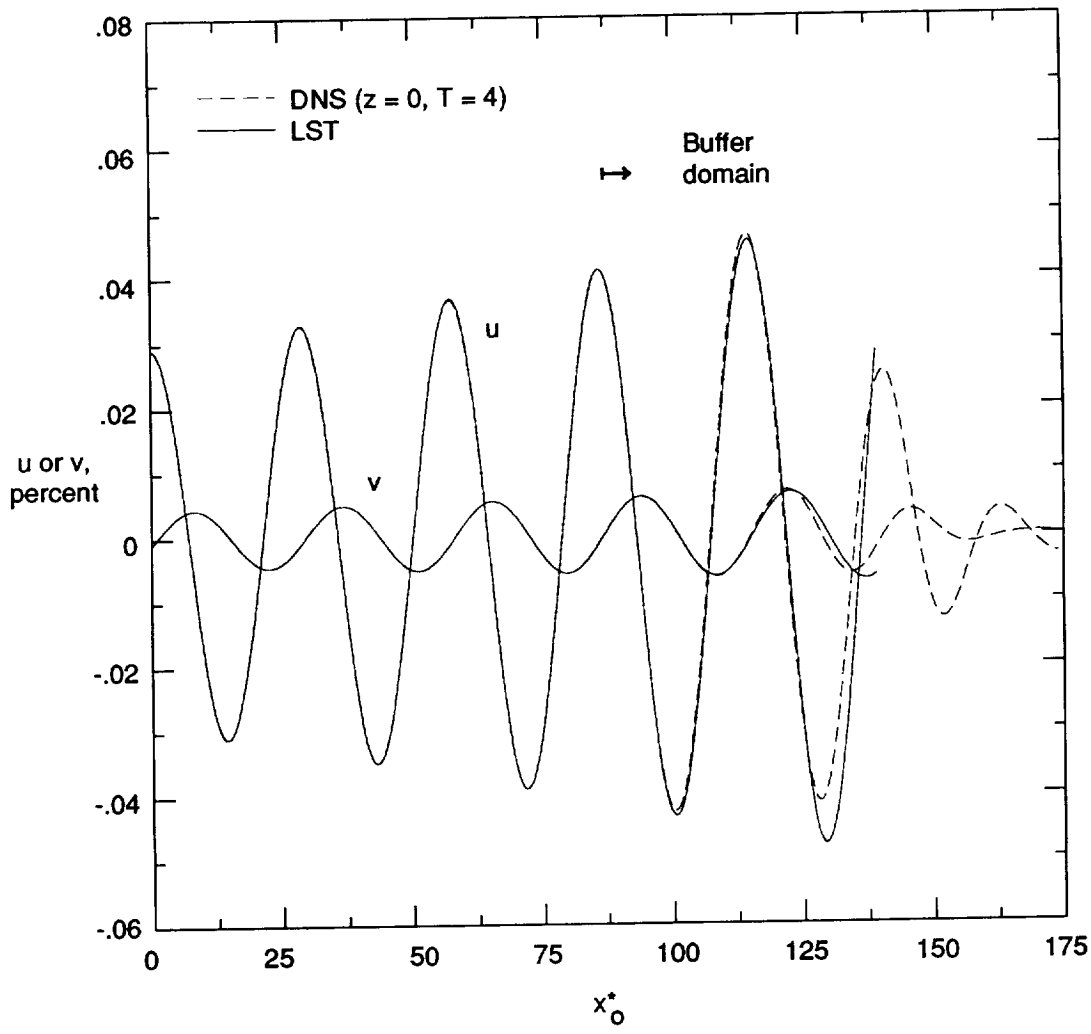

Figure 23. Streamwise and wall-normal velocity components of wave-triad disturbance with downstream distance at $z = 0$ for 3-D parallel boundary layer for inflow. $R_o^* = 900; F_r = 86; A_{1,0}^o = 0.01$ percent; $A_{1,\pm1}^o = 0.01$ percent; $\lambda_z = 20\pi$.

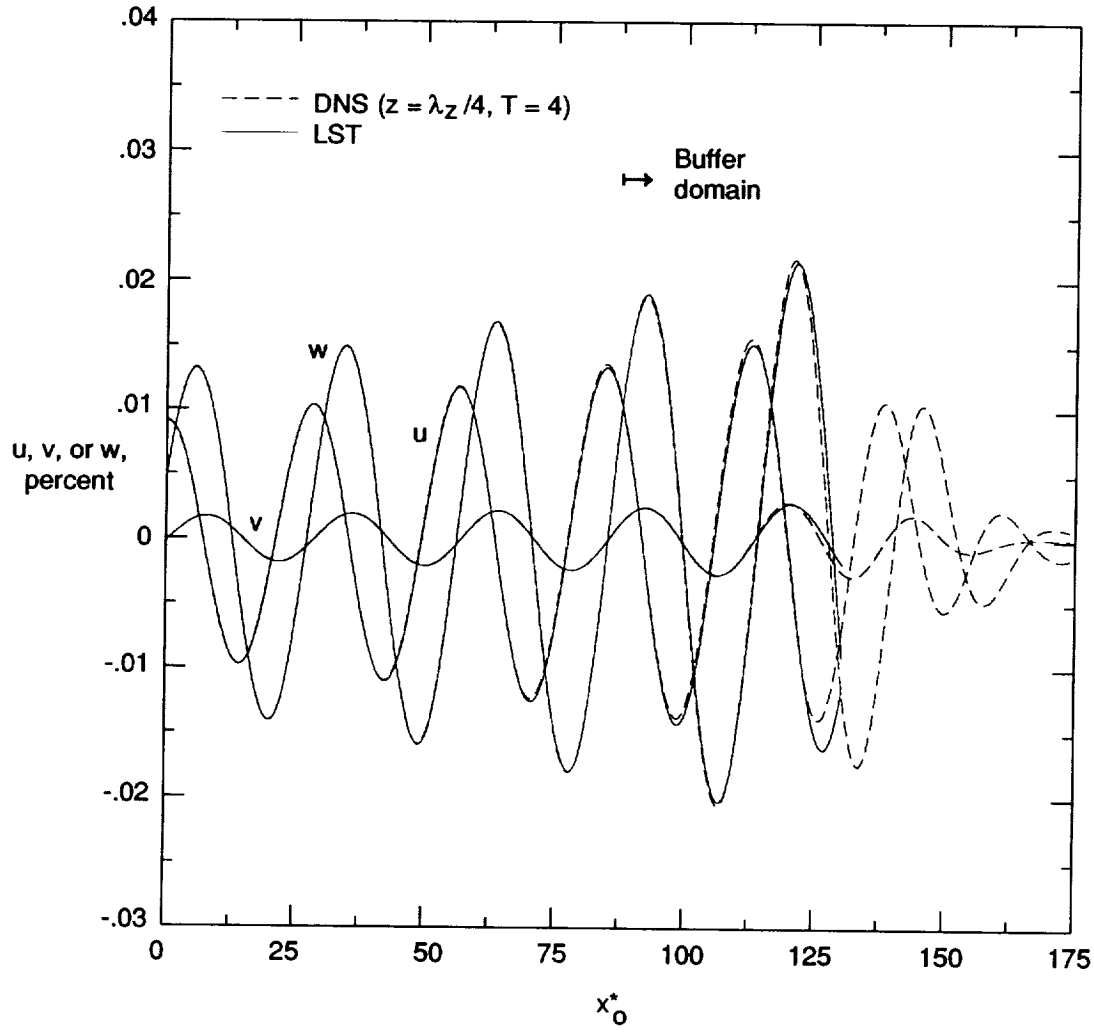

Figure 24. Streamwise, wall-normal, and spanwise velocity components of wave-triad disturbance with downstream distance at $z = \lambda_z/4$ for 3-D parallel boundary layer for inflow. $R_o^* = 900; F_r = 86$; $A_{1,0}^o = 0.01$ percent; $A_{1,\pm1}^o = 0.01$ percent; $\lambda_z = 20\pi$.

REPORT DOCUMENTATION PAGE

Form Approved
OMB No. 0704-0188

1. AGENCY USE ONLY *(Leave blank)*	2. REPORT DATE	3. REPORT TYPE AND DATES COVERED
	July 1991	Technical Paper

4. TITLE AND SUBTITLE Validation of Three-Dimensional Incompressible Spatial Direct Numerical Simulation Code
A Comparison With Linear Stability and Parabolic Stability Equation Theories for Boundary-Layer Transition on a Flat Plate

5. FUNDING NUMBERS
WU 505-59-50-01

6. AUTHOR(S)
Ronald D. Joslin, Craig L. Streett, and Chau-Lyan Chang

7. PERFORMING ORGANIZATION NAME(S) AND ADDRESS(ES)
NASA Langley Research Center
Hampton, VA 23665-5225

8. PERFORMING ORGANIZATION REPORT NUMBER
L-17026

9. SPONSORING/MONITORING AGENCY NAME(S) AND ADDRESS(ES)
National Aeronautics and Space Administration
Washington, DC 20546-0001

10. SPONSORING/MONITORING AGENCY REPORT NUMBER
NASA TP-3205

11. SUPPLEMENTARY NOTES
Joslin and Streett: Langley Research Center, Hampton, VA; Chang: High Technology Corporation, Hampton, VA.

12a. DISTRIBUTION/AVAILABILITY STATEMENT
Unclassified Unlimited

Subject Category 02

12b. DISTRIBUTION CODE

13. ABSTRACT *(Maximum 200 words)*
Spatially evolving instabilities in a boundary layer on a flat plate are computed by direct numerical simulation (DNS) of the incompressible Navier-Stokes equations. In a truncated physical domain, a nonstaggered mesh is used for the grid. A Chebyshev-collocation method is used normal to the wall; finite-difference and compact-difference methods are used in the streamwise direction; and a Fourier series is used in the spanwise direction. For time stepping, implicit Crank-Nicolson and explicit Runge-Kutta schemes are used for the time-splitting method. The influence-matrix technique is used to solve the pressure equation. At the outflow boundary, the buffer-domain technique is used to prevent convective wave reflection or upstream propagation of information from the boundary. Results of the DNS are compared with those from both linear stability theory (LST) and parabolized stability equation (PSE) theory. Computed disturbance amplitudes and phases are in very good agreement with those of LST (for small inflow disturbance amplitudes). A measure of the sensitivity of the inflow condition is demonstrated with both LST and PSE theory used to approximate inflows. Although the DNS numerics are very different than those of PSE theory, the results are in good agreement. A small discrepancy in the results that does occur is likely a result of the variation in PSE boundary condition treatment in the far field. Finally, a small-amplitude wave triad is forced at the inflow, and simulation results are compared with those of LST. Again, very good agreement is found between DNS and LST results for the 3-D simulations, the implication being that the disturbance amplitudes are sufficiently small that nonlinear interactions are negligible.

14. SUBJECT TERMS	15. NUMBER OF PAGES
Direct numerical simulation; Boundary-layer transition; Boundary-layer stability; Nonlinear boundary-layer stability; PSE theory	47
	16. PRICE CODE A03

17. SECURITY CLASSIFICATION OF REPORT	18. SECURITY CLASSIFICATION OF THIS PAGE	19. SECURITY CLASSIFICATION OF ABSTRACT	20. LIMITATION OF ABSTRACT
Unclassified	Unclassified		

NSN 7540-01-280-5500

Standard Form 298(Rev. 2-89)
Prescribed by ANSI Std. Z39-18
298-102

NASA-Langley, 1992